

Supplementary Materials for

Walking Collaborative Robots with Bimodal Skins for Adaptive Mobility Assistance

Zhibin Li¹, †, Junli Shi², †, Xinxing Chen^{3,4}, †, Xingxing Chen², †, Ping Yang⁴, Hanxiang He⁵, Yuquan Leng⁴, Xintao Huan⁶, Han Hu⁵, Chenglong Fu⁴, * , Taihong Wang^{1,*}, Chuan Fei Guo^{2,*}

¹Department of Electronic and Electrical Engineering, Southern University of Science and Technology, Shenzhen 518055, China.

²Department of Materials Science and Engineering, Southern University of Science and Technology, Shenzhen 518055, China.

³The Key Laboratory of Image Processing and Intelligent Control and the Hubei Key Laboratory of Brain-inspired Intelligent Systems, School of Artificial Intelligence and Automation, Huazhong University of Science and Technology, Wuhan 430074, China.

⁴Department of Mechanical and Energy Engineering, Southern University of Science and Technology, Shenzhen 518055, China.

⁵School of Information and Electronics, Beijing Institute of Technology, Beijing, 100081, China.

⁶School of Cyberspace Science and Technology, Beijing Institute of Technology, Beijing, 100081, China.

[†]These authors contributed equally to this work.

*To whom correspondence should be addressed. Email: fcul@sustech.edu.cn (C.F.), wangth@sustech.edu.cn (T.W.), guocf@sustech.edu.cn (C.F.G.).

This PDF file includes:

Supplementary Notes. 1 to 7

Supplementary Figs. 1 to 42

Supplementary Tables 1 to 3

References

Other Supplementary Materials for this manuscript include the following:

Supplementary Movies 1 to 7

1 **Supplementary Notes**

2 **Supplementary Note 1. Adhesion mechanism and characterization of sensor interfaces.**

3 As illustrated in **Supplementary Fig. 6(a)**, the schematic representation of the interfaces within
4 two types of sensors is provided. The sensors structure consists of four distinct interfaces, labeled
5 as Interface I (PDMS|PDMS), Interface II (PDMS|Polyimide (PI)), Interface III (Cu|Ionogel), and
6 Interface IV (Cu|PIL).

7 Adhesion Mechanism

8 The adhesion mechanisms of these interfaces are depicted in **Supplementary Fig. 6(b)**.

- 9 ● Interfaces I and II: Surface hydroxylation of PDMS and PI is achieved via air plasma treatment.
10 Upon contact, hydroxylated PDMS surfaces, as well as PDMS and PI, form Si-O-Si (Interface
11 I) and C-O-Si (Interface II) covalent bonds, respectively, facilitating strong interfacial
12 adhesion.
- 13 ● Interfaces III and IV: Copper surfaces are modified using silane chemistry. Specifically,
14 copper reacts with thiol groups from (3-Mercaptopropyl) trimethoxysilane (MPTMS) to form
15 Cu–S bonds. The Si-O-Si bonds are formed via hydrolysis reaction between the remaining
16 siloxane groups of MPTMS and siloxane groups of 3-(trimethoxysilyl) propyl methacrylate
17 (TMSPMA), anchoring acrylic ester moieties onto the copper surface. This functionalization
18 enables covalent bonding between PIL/ionogel and copper via a photo-initiated click reaction,
19 ensuring robust adhesion.

20 Characterization of Interfacial Properties

21 As illustrated in **Supplementary Fig. 6(c)**, the interfacial toughness $\Gamma(\text{J}\cdot\text{m}^{-2})$ is quantified using
22 a 180° peeling test. The toughness is determined according to Equation (1-1).

$$23 \quad \Gamma = \frac{F \cdot (1 - \cos\theta)}{d} \quad (1 - 1)$$

24 The interfacial toughness Γ is determined using a 180° peeling test, where:

- 25 ● F represents the force at which the peeling process reaches a steady state.
- 26 ● d denotes the width of the sample.
- 27 ● θ is the peeling angle, which is 180° in this case.

28 As shown in **Supplementary Fig. 6(d)**, the peeling curve of Interface III is presented as an
29 example. The blue curve corresponds to the unmodified interface, serving as the control group,
30 while the red curve represents the peeling behavior of the modified sample. Additionally,

1 **Supplementary Fig. 6(e)** compares the interfacial toughness between the control group and the
2 modified sample. The results indicate a significant increase in toughness following surface
3 modification. A stable interface is essential for ensuring the long-term durability of the electronic
4 skin, particularly under extreme conditions such as loaded under high shear forces.

1 **Supplementary Note 2. Fabrication process of bimodal iontronic skin.**

2 The production process of bimodal iontronic skin is illustrated in **Supplementary Fig. 7**. The
3 fabrication process consists of three primary stages: (1) fabrication of the electrode layer, (2)
4 fabrication of the temperature sensors, and (3) fabrication of the pressuresensors.

5 **(1) Fabrication of the Electrode Layer**

6 The process begins with exposing the surface-modified PI side, followed by spin-coating a
7 PDMS precursor onto its surface. The component is then cured at 80 ° C for 2 hours to ensure
8 complete polymerization of PDMS. Subsequently, the copper layer is exposed upwards, and the
9 electrode pattern is defined using laser cutting. After removing excess materials, the pattern is
10 transferred from the glass substrate using water transfer tape. At this stage, the PDMS side
11 becomes exposed upwards. The tape and a separate PDMS film are then plasma-treated
12 simultaneously before being pressed together to achieve adhesion. Finally, the stretchable
13 electrode layer is obtained by removing the water transfer tape via water washing.

14 **(2) Fabrication of the Temperature Sensors**

15 The electrode layer designated for temperature sensing is first immersed in a solution for
16 surface modification, followed by sequential washing with ethanol and deionized water. The
17 treated electrode layer is then placed flat on a glass substrat, and PIL precursor is squeezed at the
18 pixel positions via 3D printer and subsequently cured under UV light. Finally, the electrode layer
19 with solidified PIL and a pre-cured PDMS film used for encapsulation undergo simultaneous
20 plasma treatment, and then pressed together for adhesion, completing the temperature sensors
21 fabrication.

22 **(3) Fabrication of the Pressure-Sensitive Skin**

23 The surface modification process follows the same steps as described above. A polyethylene
24 terephthalate (PET) mask with through-holes aligned to the pixel positions is placed on the bottom
25 electrode layer. The ionogel precursor is then deposited onto the electrode surface using a scraper,
26 ensuring that the precursor infuses into the through-holes. Next, a template is placed over the
27 ionogel precursor to build microstructure on iongel surface, and the polymerization of ionogel is
28 initiated using UV light. After curing, the template and PET mask are removed. The entire
29 component, along with a PDMS spacer (used for maintaining uniform initial values for pressure
30 sensors) undergo plasma treatment , and immediately pressed together for adhesion. Finally, the
31 patterned top electrode, the bottom electrodes with attached spacer and microstructured-ionogel,

1 are encapsulated using the same adhesion method as mentioned above to complete the fabrication
2 of the pressure sensors.

3 Assembly of bimodal iontronic skin. The temperature sensors and pressure sensors are
4 subjected to plasma treatment and then pressed together, forming the bimodal iontronic skin.

Supplementary Note 3. Calculation of capacitance measurement under frequency coding architecture.

3 As shown in **Supplementary Fig. 13**, the output voltage of the capacitance-to-voltage converter
 4 (C/V converter) can be expressed as follows²:

$$V'_j(t) = \sum_{i=1}^N -\frac{R_f}{j\omega_i C_f R_f + 1} \cdot j\omega_i C_i \cdot V_i(t) \quad (2-1)$$

6 where $V'_j(t)$ is the output signal of the C/V converter on the column interface number j . ω_i is the
 7 angular frequency of the excitation source, encoding excitation row number i . N is the total
 8 number of encoding channels. R_f and C_f are the feedback resistance and capacitance. C_i is the
 9 capacitance on the different column addresses being measured, which can be expressed by solving
 10 the corresponding frequency path voltage amplitude:

$$C_i = \left| -\frac{j\omega_i C_f R_f + 1}{j\omega_i V_i(t) R_f} \right| \cdot V_j^i(t) = \frac{\sqrt{(\omega_i C_f R_f)^2 + 1}}{\omega_i R_f} \cdot \frac{A_j^i}{A_i} \quad (2-2)$$

12
 13 where $A_i = 200$ mv is the amplitude of the input AC excitation voltage signal $V_i(t)$ with angular
 14 frequency $\omega_i = 2\pi f_i^{freq}$, and A_j^i is the amplitude of the output AC signal $V_j^i(t)$ with angular
 15 frequency ω_i . Wherein, A_j^i can be demodulated and solved according to FFT (see **Supplementary**
 16 **Fig. 14**). A_j^i is the amplitude of a signal with a frequency of f_i^{freq} .

1 **Supplementary Note 4. Development of the data acquisition circuit.**

2 **Supplementary Fig. 15** and **Supplementary Fig. 16** illustrate the design block diagram and the
3 implementation of the data acquisition circuit, respectively. The data acquisition board consists of
4 five key modules: (1) control module, (2) excitation signal encoding module, (3) signal
5 demodulation module, (4) power supply module, and (5) communication module.

6 **(1) Control Module**

7 The control module comprises a microcontroller unit (MCU), a crystal oscillator, and a reset
8 circuit. The selected microcontroller, STM32H723VGH6 (STMicroelectronics), operates at a
9 clock frequency of 550 MHz, providing the computational capability required for high-speed data
10 acquisition, demodulation calculations, and data transmission. Its primary function is to perform
11 fast Fourier transform (FFT) on mixed-frequency signals to demodulate and compute the
12 capacitive responses at different excitation frequencies.

13 **(2) Excitation Signal Encoding Module**

14 The Direct Digital Synthesizer (DDS), AD9833 (Analog Devices), generates the alternating
15 current (AC) frequency-encoded excitation signals. The output is processed by a backend
16 operational amplifier and a high-pass filter, yielding a voltage amplitude of 200 mV.

17 **(3) Power Supply Module**

18 The data acquisition circuit is powered by a 5V USB source. Within the power supply module:
19 A Low Dropout Regulator (LDO) ensures a stable conversion of 5V to 3.3V to power the MCU.
20 A DC-DC converter generates -5V to supply the operational amplifier's negative rail.

21 **(4) Signal Demodulation Module**

22 The C/V converter employs the precision operational amplifier OPA4388 (Texas Instruments)
23 to convert capacitance variations into corresponding voltage signals. These signals are digitized
24 using a 16-bit Analog-to-Digital Converter (ADC), AD7606 (Analog Devices), which features 8
25 channels and a maximum conversion rate of 200 kSPS, ensuring accurate voltage signal
26 acquisition for subsequent demodulation calculations. An analog switch matrix (CH446Q, WCH)
27 enables channel switching within the temperature sensor array.

28 **(5) Communication Module**

29 The acquired data is then transmitted from the microcontroller to a local server or PC via
30 USB or WiFi (facilitated by the RF communication chip EMC3090).

Supplementary Note 5. Control parameters in the apparent dynamic model.

Walking collaborative robots require the ability to provide positive feedback based on perceived tactile information to better adapt to tasks or users⁴. The general motion control algorithm for the walking assistance robot based on passive behavior is implemented by applying imposed apparent dynamics^{5,6}. These apparent dynamics can be considered as the desired, where the robot's walking assistance behavior is guided by the user's intentions⁷. The admittance control equation is shown in Equation (1).

$$M_d \ddot{\phi}_r + D_d \dot{\phi}_r = F_m \quad (1)$$

9 where \mathbf{M}_d and \mathbf{D}_d are the desired inertia and damping matrices, respectively. The state vector of
 10 robot, $\varphi_r = [x \ \theta]^T$, includes the displacement x in the forward direction and the turning angle θ ,
 11 which denotes the deviation of the collaborative robot from its forward direction. The human
 12 motion intention is described by \mathbf{F}_m , representing the applied force F_x in the forward direction and
 13 the torque T_z to the walking collaborative robot (see **Supplementary Fig. 29**). The structure of
 14 \mathbf{M}_d , \mathbf{D}_d and \mathbf{F}_m are given by Equations (2) - (4), respectively:

$$\boldsymbol{M}_d = \begin{bmatrix} M_x & 0 \\ 0 & M_\theta \end{bmatrix} \quad (2)$$

$$\mathbf{D}_d = \begin{bmatrix} D_x & 0 \\ 0 & D_\theta \end{bmatrix} \quad (3)$$

$$\mathbf{F}_m = [F_x \ T_z]^T \quad (4)$$

where M_x and D_x represent the desired inertia and damping coefficients in the forward displacement x , respectively, and M_θ and D_θ represent the desired inertia and damping coefficients for the steering angle θ , respectively. The vertical force F_z represents the support force during the assistance interaction, which is used to assess the support provided by the collaborative robot to the user. \mathbf{F}_h as the critical control information that ensures the desired dynamics during human interaction and assistance with the walking collaborative robot, serving as the prediction target for MI, with $\mathbf{F}_h \in [F_x, F_z, T_z]$. Therefore, the precise sensing and inference of \mathbf{F}_h by the walking collaborative robot equipped with iontronic skins is of paramount importance.

1 Supplementary Note 6. Description of the Vector Mechanics Model.

In hybrid motion intention model (HMIM), the vector mechanics model (VMM) is a physical model that encapsulates prior physical knowledge³. This model relies on the normal forces measured by each pressure sensor unit embedded in the iontronic skins. Using the rotation matrix \mathbf{R}_s , these forces are spatially remapped to compute the resultant force, denoted as \mathbf{F}_h .

$$F_h = R_s \cdot f_s \quad (3-1)$$

where, \mathbf{f}_s represents the normal pressure measured by each pressure sensor unit on the iontronic skins, $\mathbf{f}_s \in \mathbb{R}^{768 \times 1}$. The rotation matrix R_s can be obtained from the CAD model of the walking collaborative robot equipped with bimodal skins, where $\mathbf{R}_s \in \mathbb{R}^{3 \times 768}$ (the solving process is shown in **Supplementary Fig. 30**).

The VMM is a form of prior physical knowledge. This model neglects the positional errors of the actual sensor attachment, sensor consistency errors, and mechanical structural errors. It relies on the normal forces measured by each sensor unit on the bimodal skins and uses spatial mechanics decomposition to solve the interaction forces in the x and z directions by spatially remapping them. As shown in **Supplementary Fig. 30**, given the known positions and angles α_i of the attached sensors, the normal force f_i of each sensor is decomposed into the x and z directions:

$$F_{x,i} = f_i \cdot \cos(\alpha_i) \quad (3-2)$$

$$F_{z,i} = f_i \cdot \sin(\alpha_i) \quad (3-3)$$

21 Calculate the resultant force in the x and z directions for the entire set of sensors. The resultant
22 force in the x direction for the left armrest is:

$$F_{x_left} = \sum_{i=1}^{N/2} F_{x,i} = \sum_{i=1}^{N/2} f_i \cdot \cos(\alpha_i) \quad (3-4)$$

24 where $1 \sim N/2$ represents the sensing units on the left armrest.

25 The resultant force in the x direction for the right armrest is:

$$F_{x_right} = \sum_{i=\left(\frac{N}{2}+1\right)}^N F_{x,i} = \sum_{i=\left(\frac{N}{2}+1\right)}^N f_i \cdot \cos(\alpha_i) \quad (3-5)$$

27 where $(\frac{N}{2} + 1) \sim N$ represents the number of sensing units on the right armrest.

1 The resultant force in the x direction under overall support is:

2

$$F_x = F_{x_{left}} + F_{x_{right}} = \sum_{i=1}^N f_i \cdot \cos(\alpha_i) \quad (3 - 6)$$

3

4 The resultant force in the z direction under overall support is:

5

$$F_z = \sum_{i=1}^N f_i \cdot \sin(\alpha_i) \quad (3 - 7)$$

6 The rotational torque under overall support is:

7

$$T_z = (F_{x_{right}} - F_{x_{left}}) \cdot L = \left(\sum_{i=\left(\frac{N}{2}+1\right)}^N f_i \cdot \cos(\alpha_i) - \sum_{i=1}^{\frac{N}{2}} f_i \cdot \cos(\alpha_i) \right) \cdot L \quad (3 - 8)$$

8 L represents the distance between the center points of the left and right bimodal skins and the
9 center of the support robotic arm (see **Supplementary Fig. 30(d)**).

10 Based on equations (3-6) to (3-8), the collection of sensor units $\mathbf{f}_s \in \mathbb{R}^{768 \times 1}$, after spatial
11 remapping, can be used to determine $\mathbf{F}_h \in [F_x, F_z, T_z]$.

12

$$\mathbf{F}_h = \mathbf{R}_s \cdot \mathbf{f}_s \quad (3 - 9)$$

13 where $\mathbf{R}_s \in \mathbb{R}^{3 \times 768}$ is the rotation matrix coefficient in equations (3-6) to (3-8), obtained from the
14 CAD model of the sensor attachment spatial positions.

15

1 **Supplementary Note 7. Description of the dataset based on walking collaborative robot.**

2 To develop and train an inference model for human movement intentions (MI) and interactive
3 dynamic gestures (DG) under the distributed pressure mapping of bimodal skins, we collected a
4 large-scale dataset from a walking collaborative robot. This dataset consists of two subsets: (1) an
5 MI dataset recorded during assisted walking and (2) a DG dataset collected under touch
6 interactions.

7 **(1) MI Dataset: Assisted Walking Interaction**

8 The MI dataset comprises distributed tactile pressure data captured by bimodal skins, along
9 with six-axis force/torque sensor data, recorded at 40 Hz over more than 200,000 frames.
10 Participants simulated intended interactive forces based on various motion path prompts.

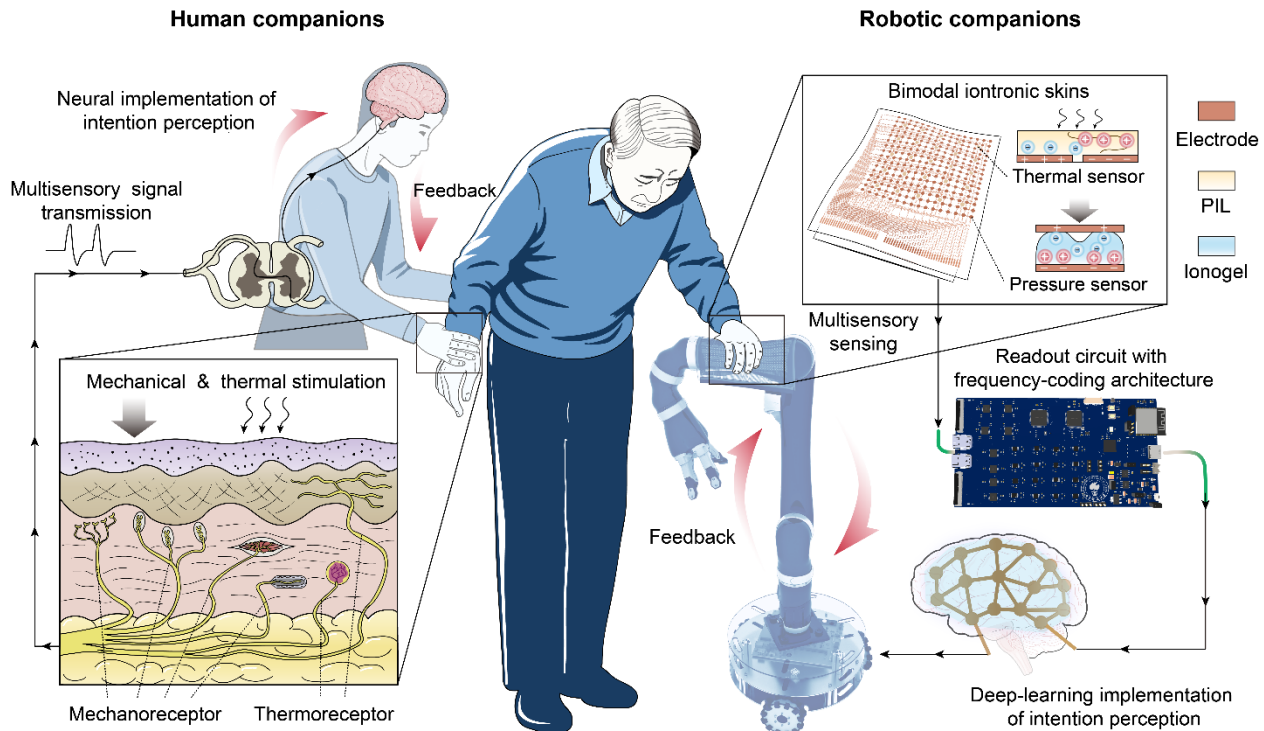
- 11 • Data was collected from 12 participants of varying ages and movement habits.
- 12 • Each participant completed four rounds of data collection (**Supplementary Fig. 33a**).
- 13 • During the experiment, the robot remained stationary under high damping to prevent
14 movement.
- 15 • Participants were given motion path prompts, guiding them to apply intended control
16 interaction forces to the assistive robot.
- 17 • Data from the bimodal skin and six-axis force/torque sensors were recorded for corrective
18 learning.

19 **(2) DG Dataset: Dynamic Touch Interaction**

20 The DG dataset includes tactile data captured by bimodal skins from 12 participants, each
21 performing 11 distinct dynamic touch gestures. The dataset consists of more than 50,000 frames,
22 recorded at 40 Hz, with each gesture repeated four times (**Supplementary Fig. 33b**).

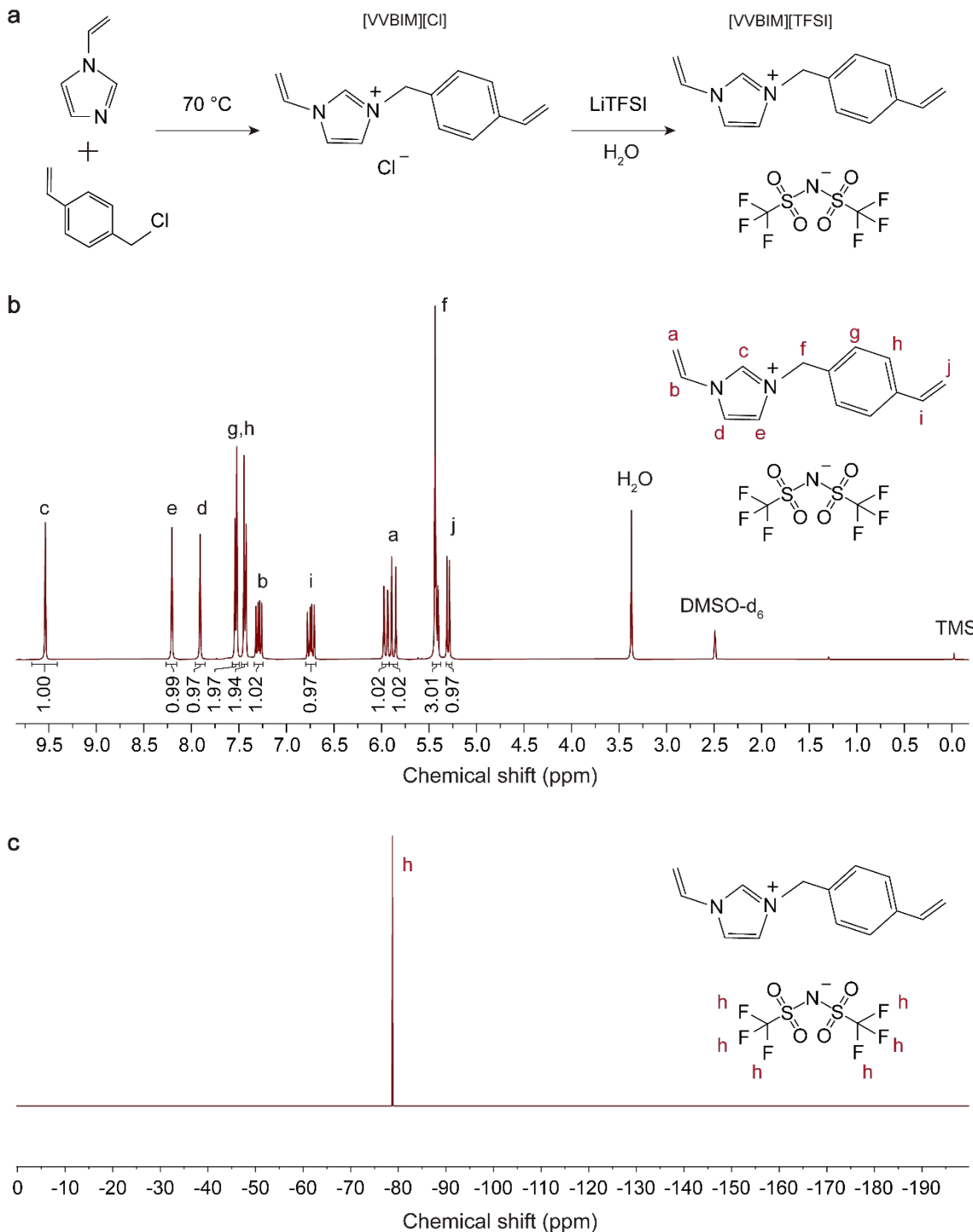
23 For cross-validation among participants, we selected data from two users as the test dataset
24 and performed 6-fold cross-validation across all users, reporting the average results.

1 **Supplementary Figures**

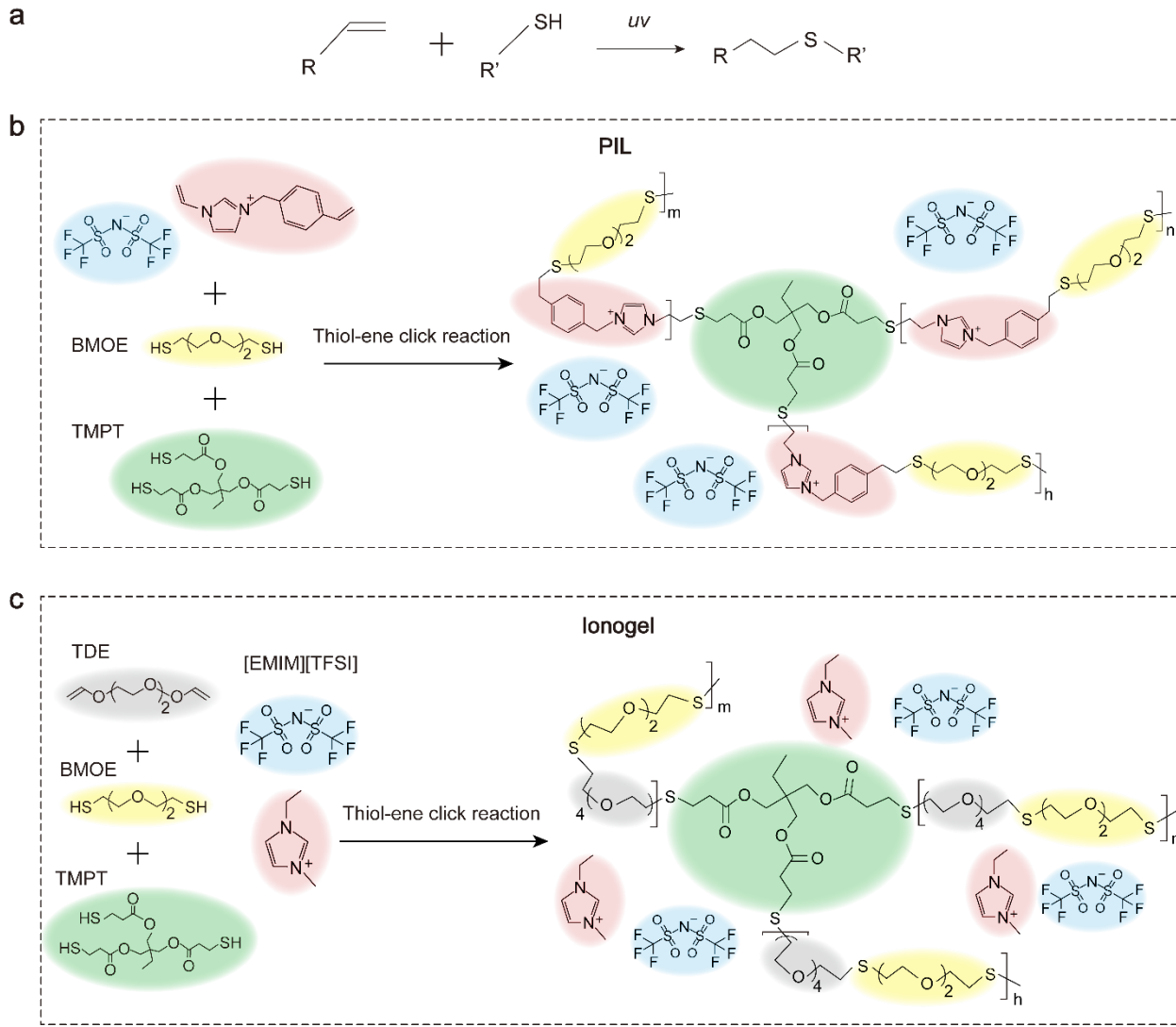


2

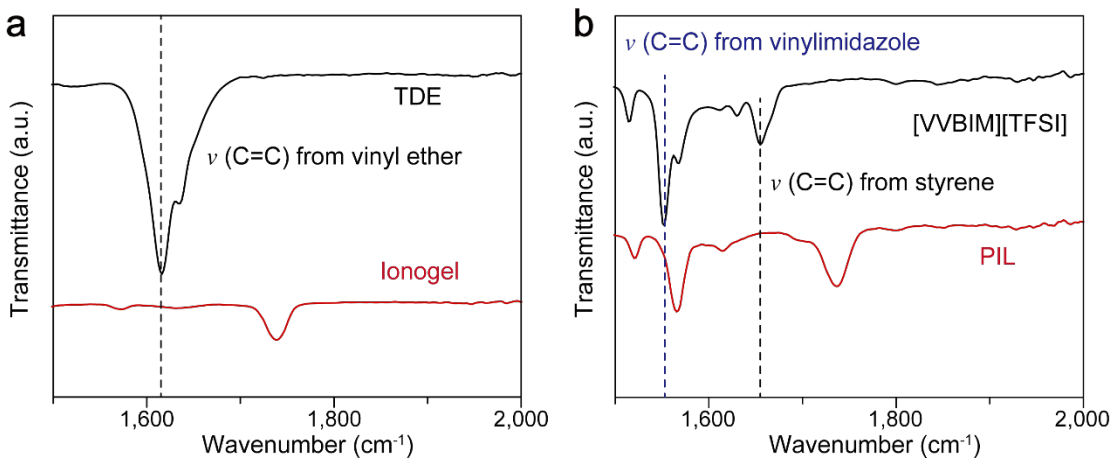
3 **Supplementary Figure 1. An overview of walking collaborative robot equipped with bimodal iontronic skins.** A schematic illustration of the robot's design concept, comparing its architecture and artificial distributed multisensory inference system to the human multisensory perception and mobility assistance system.



2 **Supplementary Figure 2. Synthesis of diolefin ionic liquid monomer (1-vinyl-3-(4-**
3 **vinylobenzyl)imidazolium bis(trifluoromethylsulfonyl)imide ([VVBIM][TFSI]). (a)** synthetic
4 **flow chart of [VVBIM][TFSI]. (b)** 1H-NMR spectrum (400 MHz, Dimethyl sulfoxide-d₆, 298K)
5 δ(ppm): 9.53(s,1H), 8.20 (dt, 1H), 7.91(dt,1H),7.53(dd, 2H), 7.43(dd, 2H), 7.29(dd, 1H), 6.74(dd,
6 1H), 5.95(dd, 1H), 5.87(d, 1H), 5.43(s, 2H), 5.42 (dd, 1H), 5.29 (d, 1H). **(c)** F19-NMR spectrum.
7



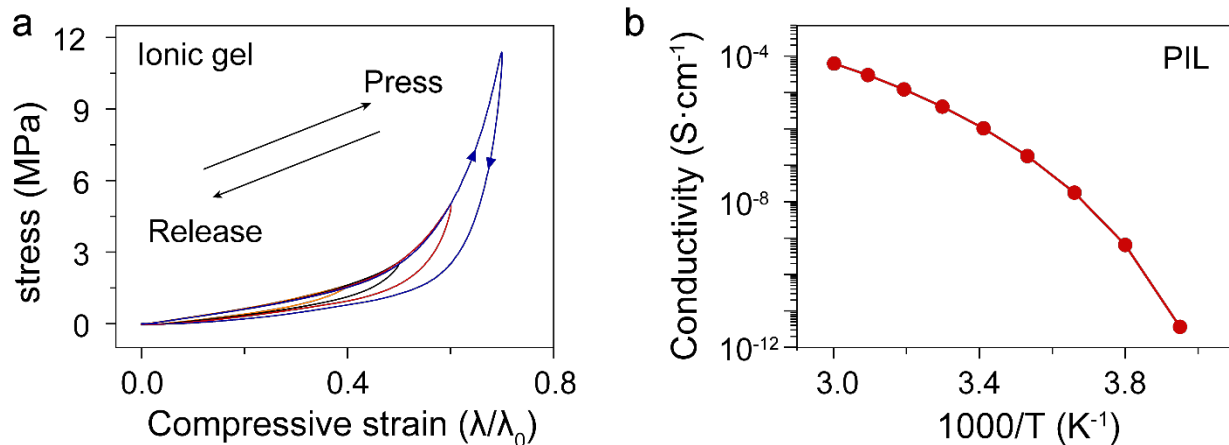
1 **Supplementary Figure 3. Thiol-ene click reaction mechanism and polymerization process of**
2 **ionic crosslinked polymer utilized for our sensor.** (a) Thiol-ene click reaction mechanism. The
3 carbon-sulfur bond is formed by the click reaction between the thiol group and the -ene group from
4 alkene via photoinitiation⁸. (b) The reaction mechanism of poly-ionic liquid (PIL). The diolefin
5 ionic liquid monomer ([VVBIM][TFSI], details see **Supplementary Fig. 2**), dithiol monomer
6 (1,2-bis (2-mercaptoethoxy) ethane (BMOE)) and trithiol crosslinker (trimethylolpropane tris (3-
7 mercaptopropionate) (TMPT)) are mixed together with the mole ratio 1:1 between ene and thiol
8 group, and the crosslinked PIL network is formed via photo-initiated click reaction. (c) The
9 reaction mechanism of ionogel. Ionic liquid (1-ethyl-3-methylimidazolium
10 bis(trifluoromethylsulfonyl)imide [EMIM][TFSI]), diolefin monomer (tri (ethylene glycol)
11 divinyl ether (TDE)), dithiol monomer (BMOE) and trithiol crosslinker (TMPT) are mixed
12 together with the mole ratio 1:1 between ene and thiol group, and the crosslinked ionogel is formed
13 via photo-initiated click reaction.



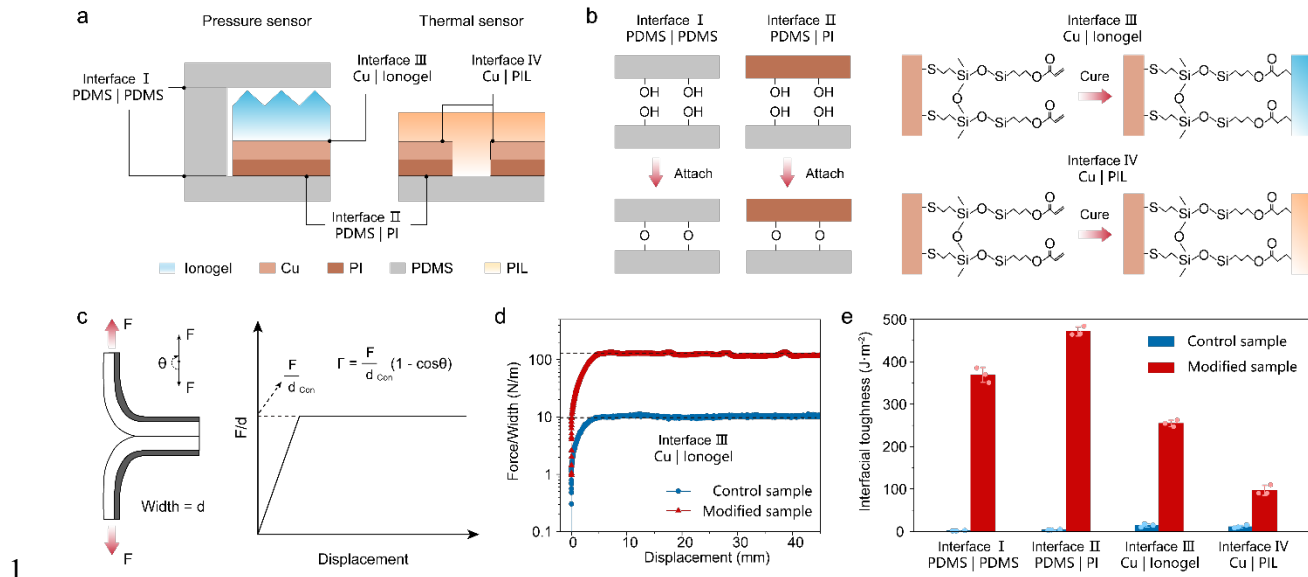
1

2 **Supplementary Figure 4. Attenuated total reflection infrared (ATR-IR) transmission**
3 **spectrum of the polymer and precursor. (a)** The ATR-IR spectra of TDE and ionogel. It is
4 observed that the fingerprint peak of $\nu(\text{C}=\text{C})$ from vinyl ether⁹ in TDE disappear after click
5 reaction, which indicates that the vinyl group reacted completely. **(b)** The ATR-IR spectra of
6 [VVBIM][TFSI] and PIL. It is observed the fingerprint peak of $\nu(\text{C}=\text{C})$ from vinylimidazole¹⁰ and
7 styrene¹¹ disappear after click reaction, which indicates that the vinylimidazole and styrene group
8 reacted completely.

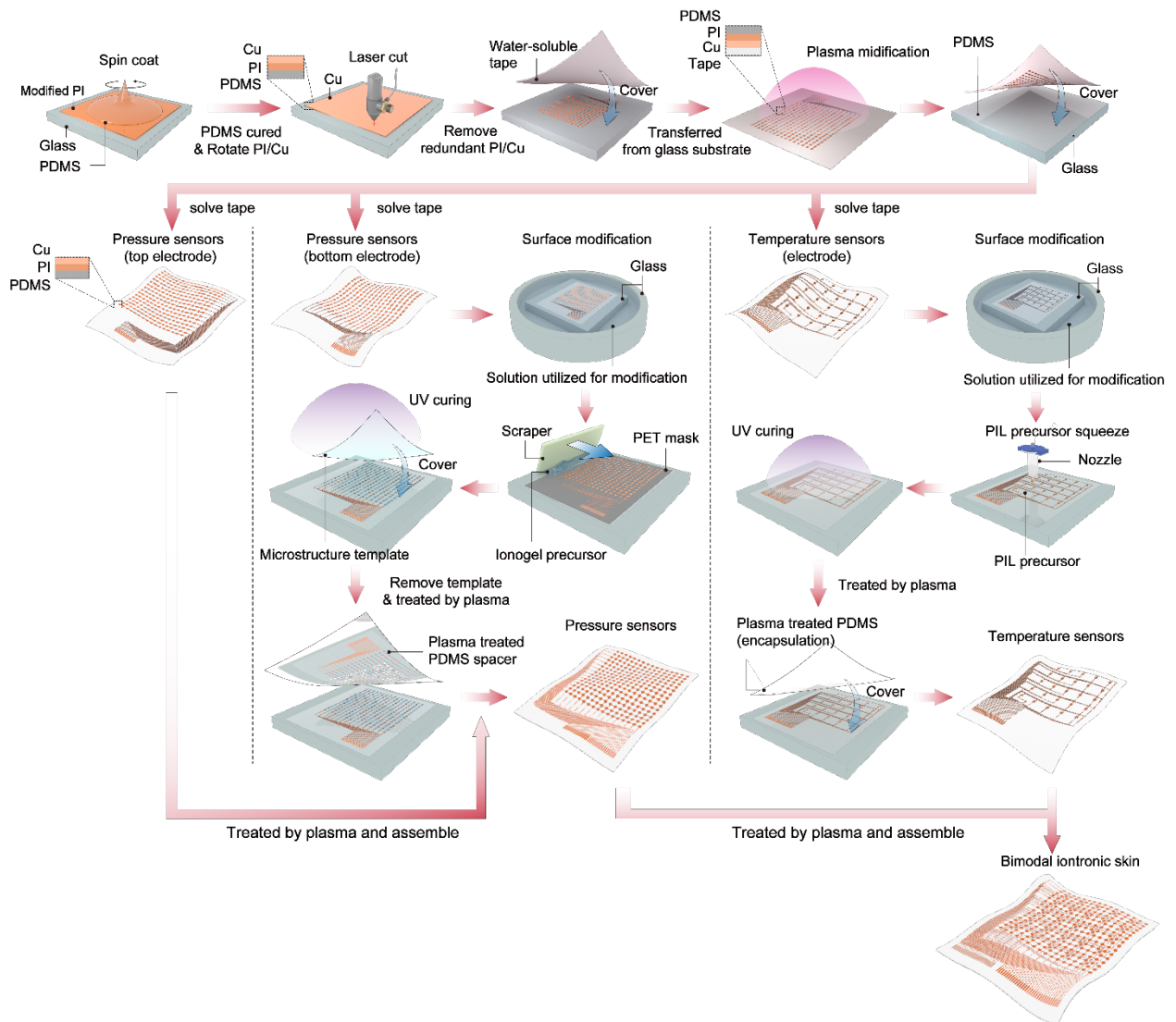
9



1
2 **Supplementary Figure 5. Characterization of ionogel and PIL.** (a) Press-release curve of
3 ionogel. The ionogel exhibits full recovery under 40%-70% compressive strain, demonstrating
4 notable resilience. This property significantly enhances the recovery performance of the pressure
5 sensor. (b) Ionic conductivity of PIL varies with temperature. The curve satisfies VTF equation¹²,
6 which demonstrates that the PIL is under high elastic state throughout the tested temperature range.
7 Besides, the conductivity spans two orders of magnitude within the practical application range (10-
8 60 ° C), facilitating the development of highly sensitive temperature sensors.
9



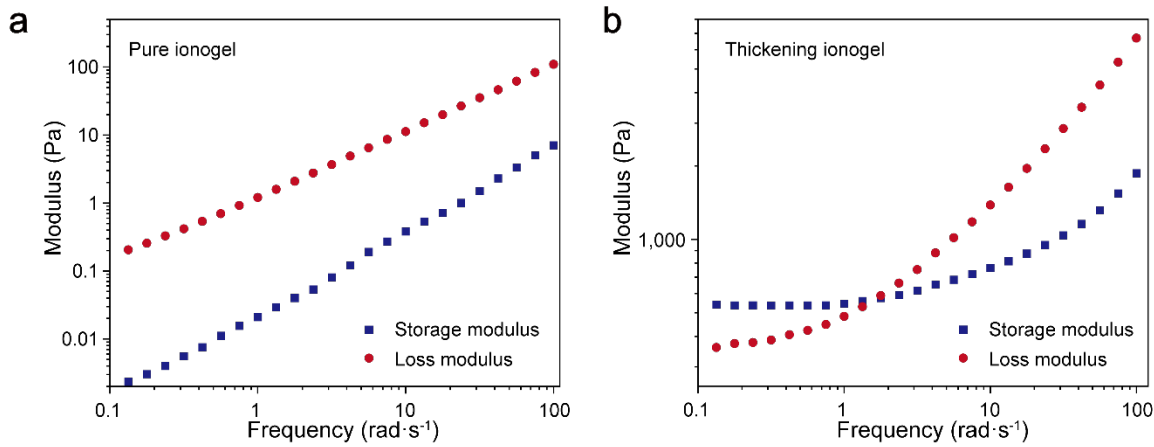
Supplementary Figure 6. The adhesion mechanism and characterization of the interfaces inside sensors. (a) The schematic of the interfaces inside two types sensors. (b) Adhesion mechanism of four types interfaces. (c) The testing principle of interface property (i.e. interfacial toughness $\Gamma(\text{J}\cdot\text{m}^{-2})$). (d) The peeling curve of interface III is used as an example. The blue one represents the peeling curve of the unmodified interface as control group, while the red curve represents the peeling curve of modified sample. (e) Interfacial toughness of control group and the sample after surface modification, while the modified interfaces demonstrate several orders improvement of interfacial toughness compared to control samples.



1

2 **Supplementary Figure 7. The fabrication process of bimodal iontronic skin.** The process can
3 be divided into three parts: the fabrication of electrode layer, temperature sensors, pressure
4 sensors respectively.

1

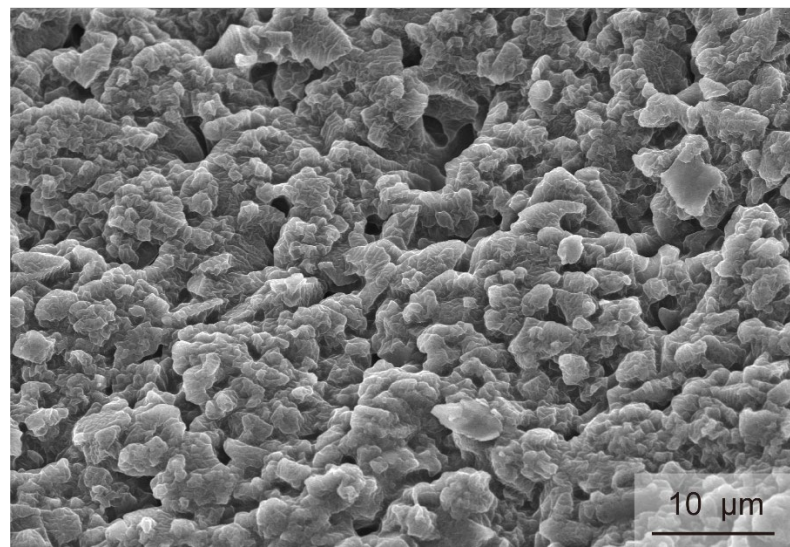


2

3 **Supplementary Figure 8. Rheological curve of ionogel precursor.** We select poly
4 (vinylidenefluoride-*co*-hexafluoropropylene (P(VDF-*co*-HFP)) to thicken the precursor of ionogel.
5 (a) The precursor without adding P(VDF-*co*-HFP) remains in a fluid state regardless of whether
6 shear force is applied. (b) The thickened precursor demonstrates shear-thinning behavior, which
7 allowing it to be easily scraped like fluid while maintaining adhesion to the designated pixel
8 positions like solid without flowing.

9

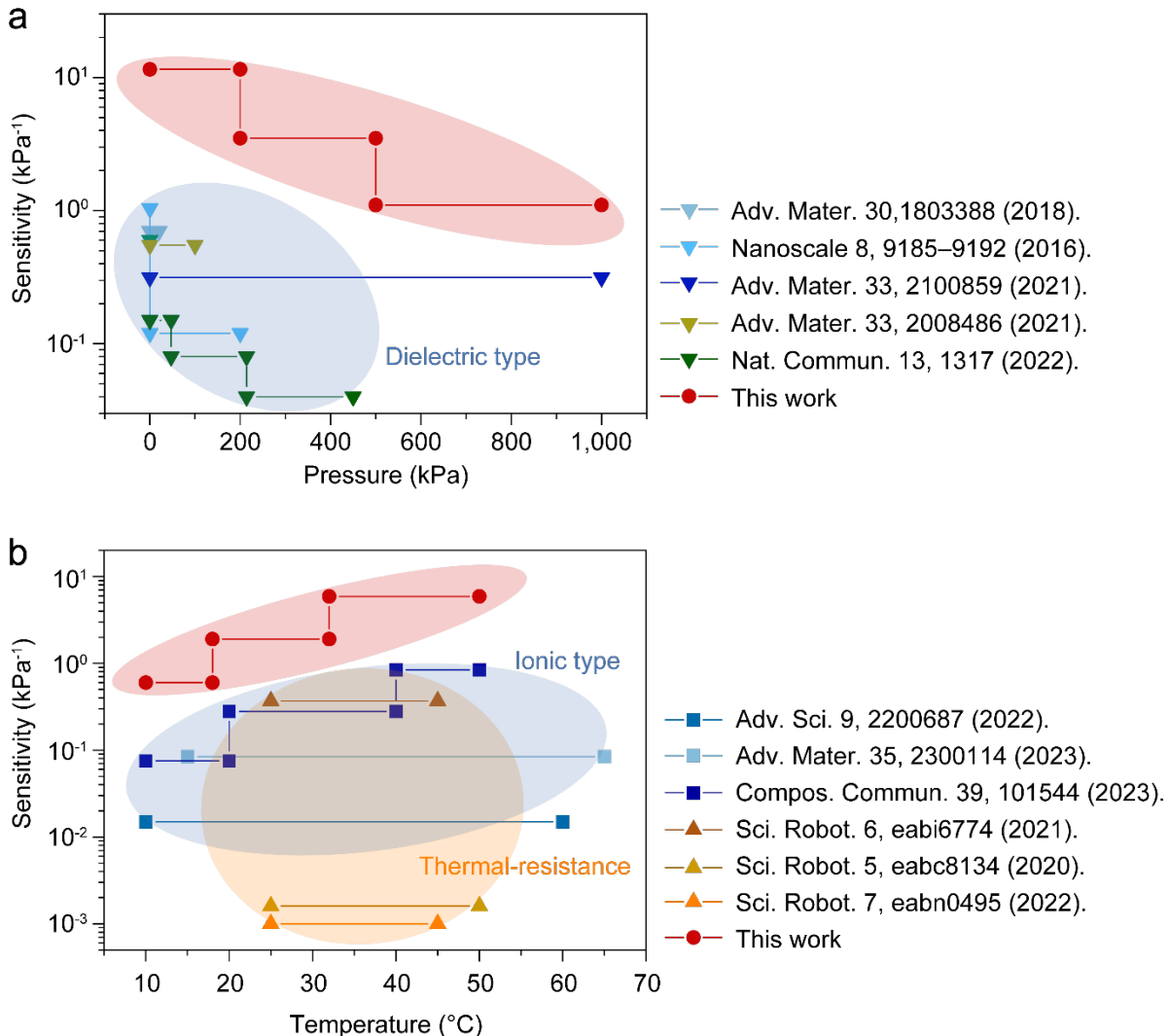
1



2

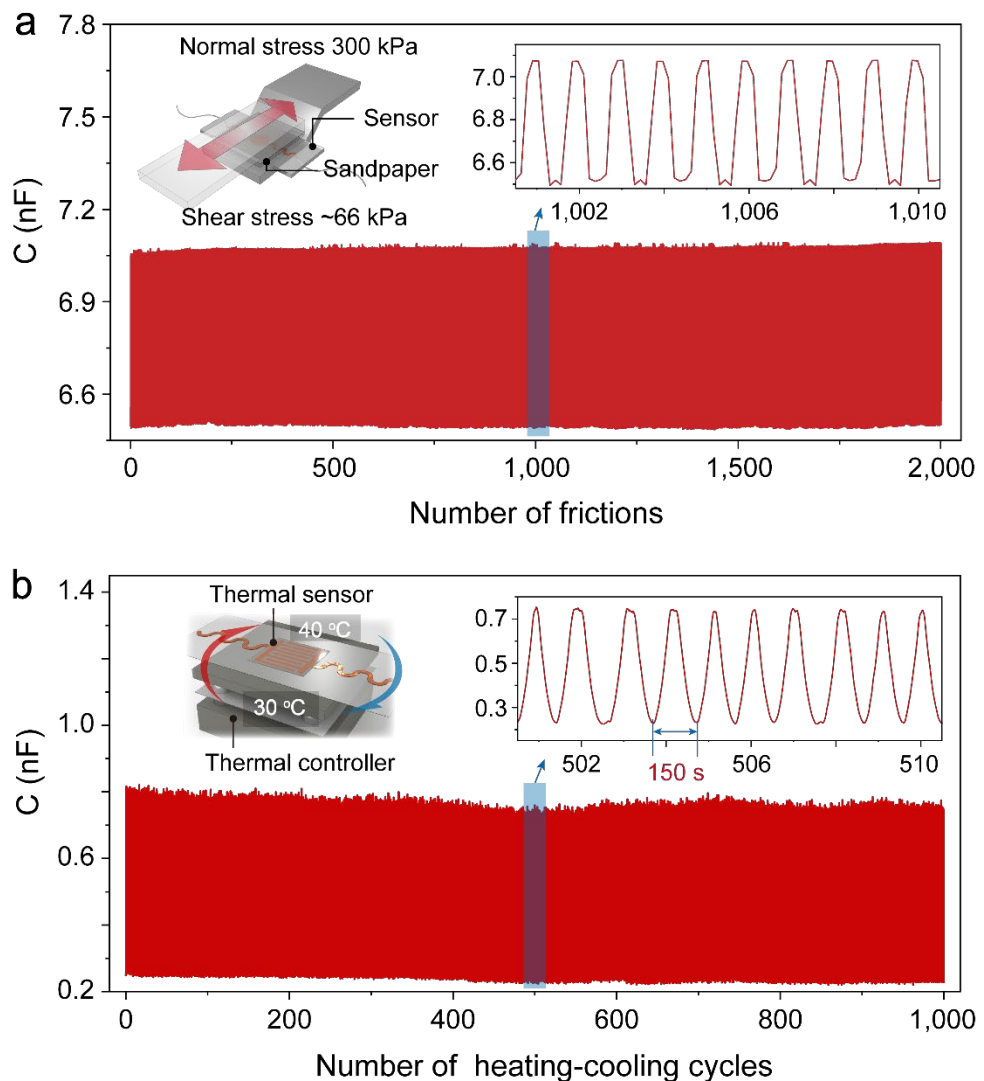
3 **Supplementary Figure 9. Scanning electron microscopy (SEM) image of the microstructure**
4 **on ionogel surface.** A microstructure with a feature size of 5–10 μm can be fabricated on the
5 surface of ionogel using soft lithography, thereby enhancing the sensitivity of the pressure sensor.

6



1

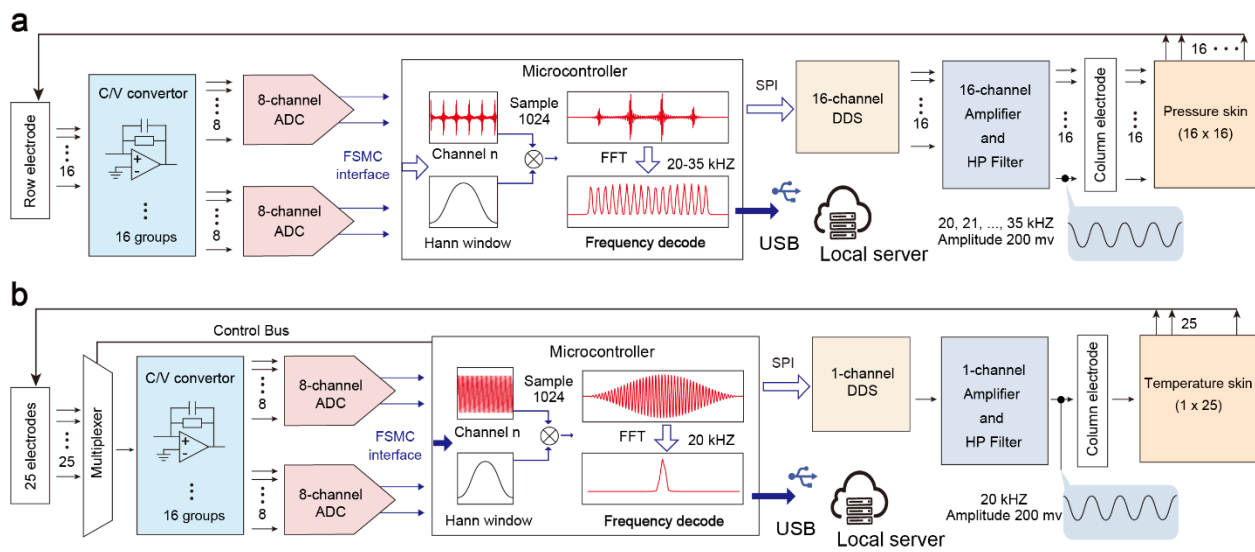
2 **Supplementary Figure 10. Sensitivity comparison of the sensors.** (a) Sensitivity comparison
3 between iontronic and dielectric pressure sensors. In iontronic sensors, the capacitance density of
4 the electrical double layer (formed at the interface between ions (ionogel) and electrons (electrodes)
5 at the nanometer scale) is significantly higher than the volumetric capacitance density of dielectric-type
6 sensors. Consequently, our iontronic pressure sensor exhibits superior sensitivity compared
7 to dielectric-type sensors. (b) For temperature sensors, ion dissociation and diffusion are more
8 responsive to temperature changes than phonon scattering in metallic materials, resulting in higher
9 sensitivity for ion-based temperature sensors. Additionally, although polymerized ionic liquid (PIL)
10 exhibits lower initial conductivity than ionogel, both materials achieve comparable conductivity
11 at high temperatures. Therefore, PIL-based temperature sensors demonstrate higher sensitivity
12 compared to ionogel-based sensors.
13



1

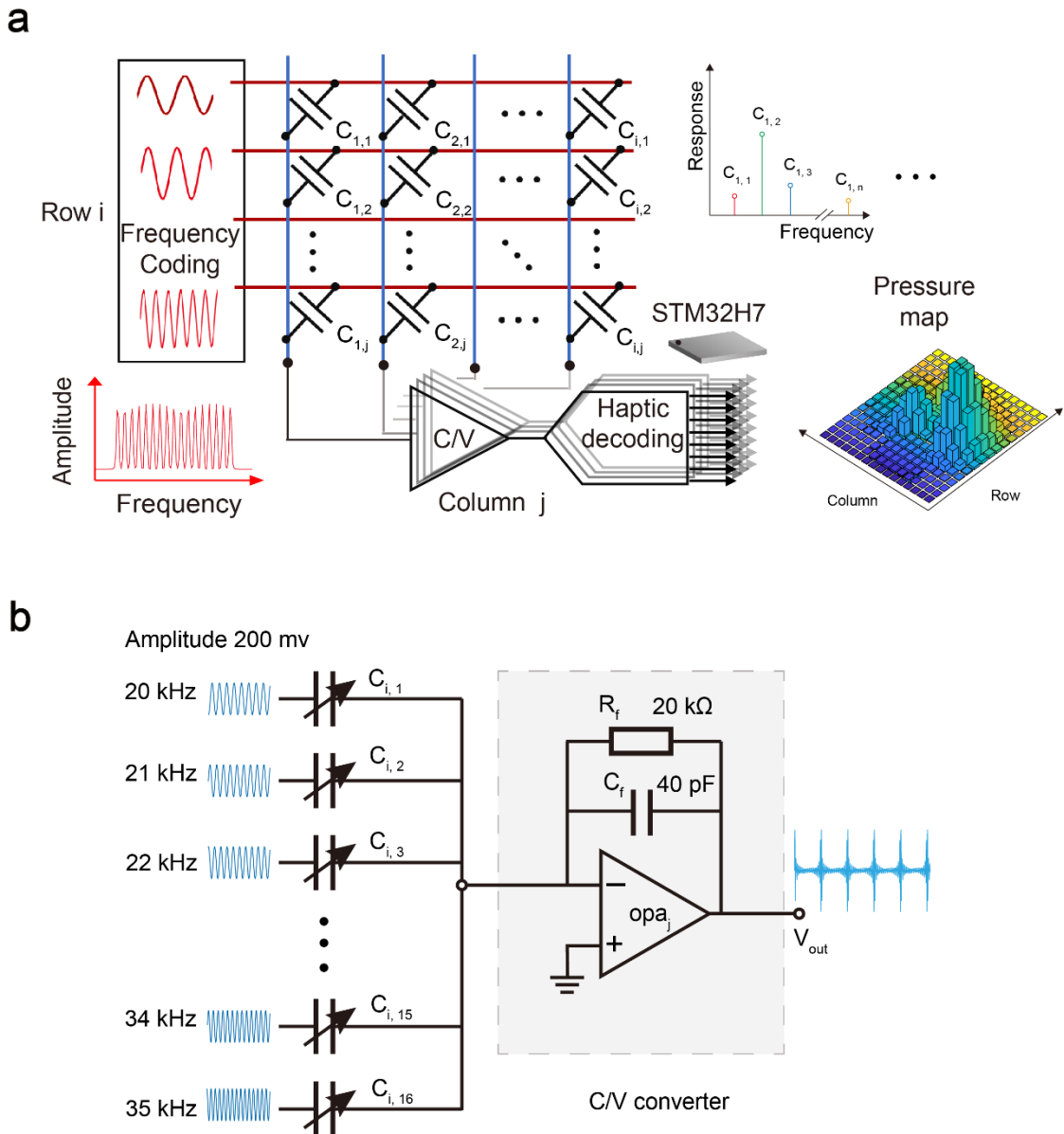
2 **Supplementary Figure 11. Cycle stability of sensors.** (a) Signal variation of the pressure sensor
 3 under cyclic tangential loading at 66 kPa (using #500 sandpaper with a friction coefficient of 0.22).
 4 The sensor demonstrates excellent cycling stability due to its strong interfacial adhesion. (b) Signal
 5 variation of the temperature sensor under cyclic temperature fluctuations in the range of 30–40 °
 6 C. The sensor exhibits outstanding cycling stability, attributed to the purely physical nature of the
 7 electrical double-layer capacitance and the entropy-driven process of ion dissociation and diffusion
 8 at different temperatures.

1

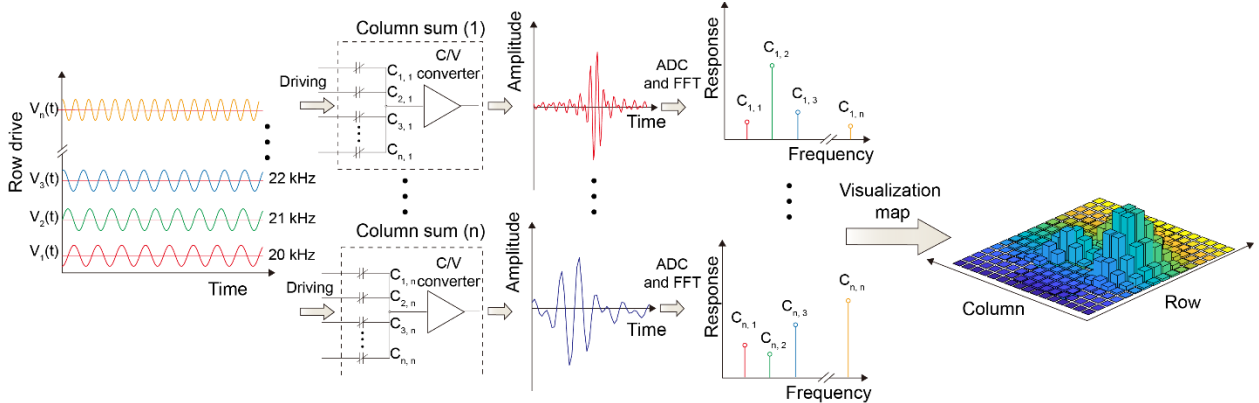


2

Supplementary Figure 12. Architectural diagram of the bimodal iontronic skin readout interface. (a) Schematic of the 16×16 iontronic pressure array architecture. Sixteen Direct Digital Frequency Synthesizers (AD9833, Analog Devices) are implemented, with backend components including operational amplifiers and high-pass filters to generate excitation signals within the frequency range of 20–35 kHz and a voltage amplitude of 200 mV. Sixteen-channel capacitance-to-voltage (C/V) converters and an analog-to-digital converter (ADC, AD7606, Analog Devices) process the voltage signals from the analog signal chain. The microcontroller then performs fast Fourier transform (FFT) demodulation on the mixed signals. (b) Schematic of the 1×25 iontronic temperature array architecture. Unlike the pressure sensor design, a single 20 kHz excitation signal is utilized, with an analog switch incorporated at the receiving end to sequentially acquire voltage signals from 25 channels. Abbreviations: DDS, direct digital synthesizer; OP-AMP, operational amplifier; HP filter, high-pass filter; C/V converter, capacitance-to-voltage converter; ADC, analog-to-digital converter; FSMC, Flexible Static Memory Controller; SPI, Serial Peripheral Interface.

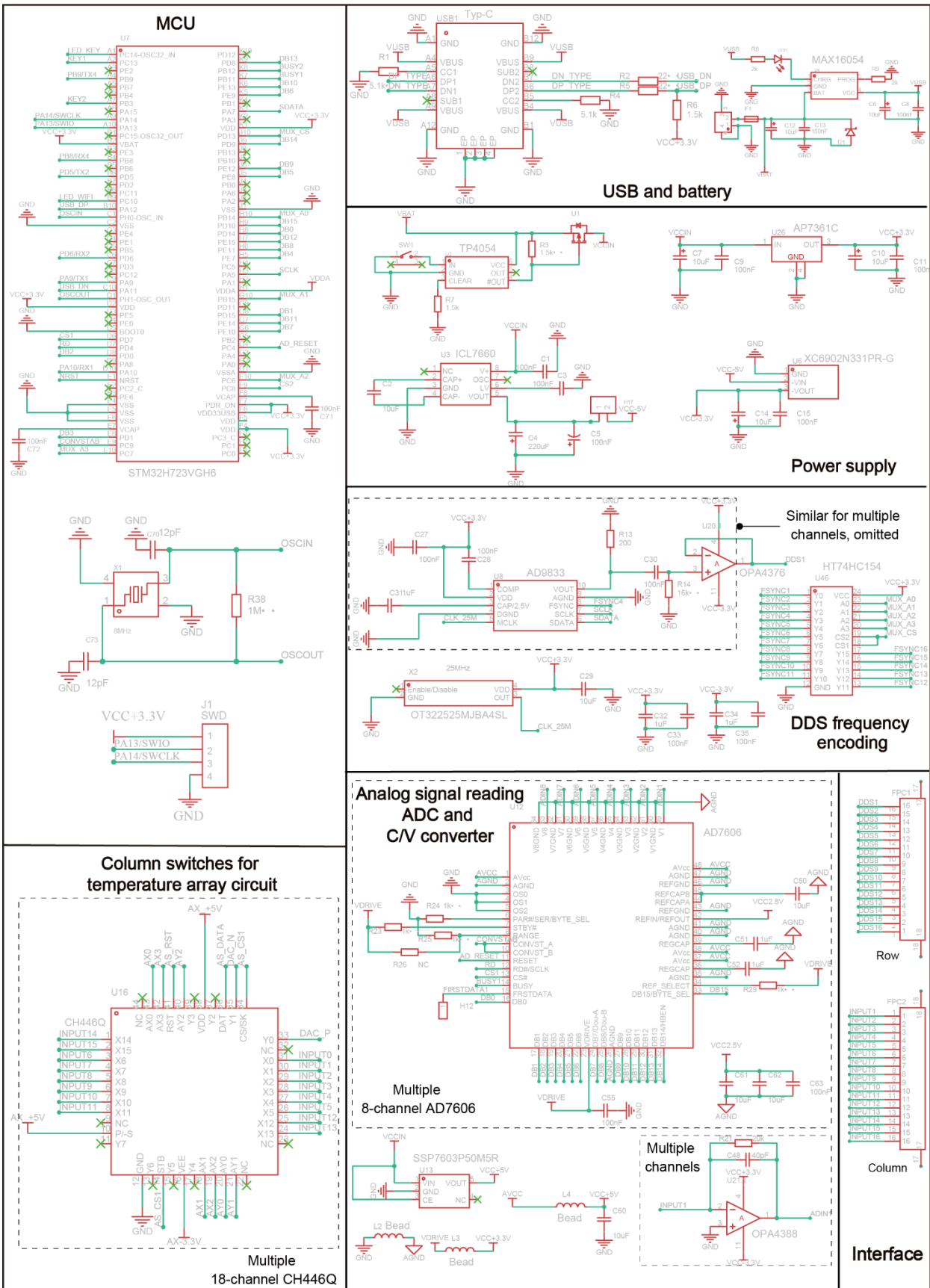


2 **Supplementary Figure 13. Calculation of capacitance measurement under the frequency
3 coding architecture. (a) System diagram of the frequency coding architecture. (b) Schematic
4 representation of the parallel summation of capacitive nodes by the capacitance-to-voltage (C/V
5 converter).**



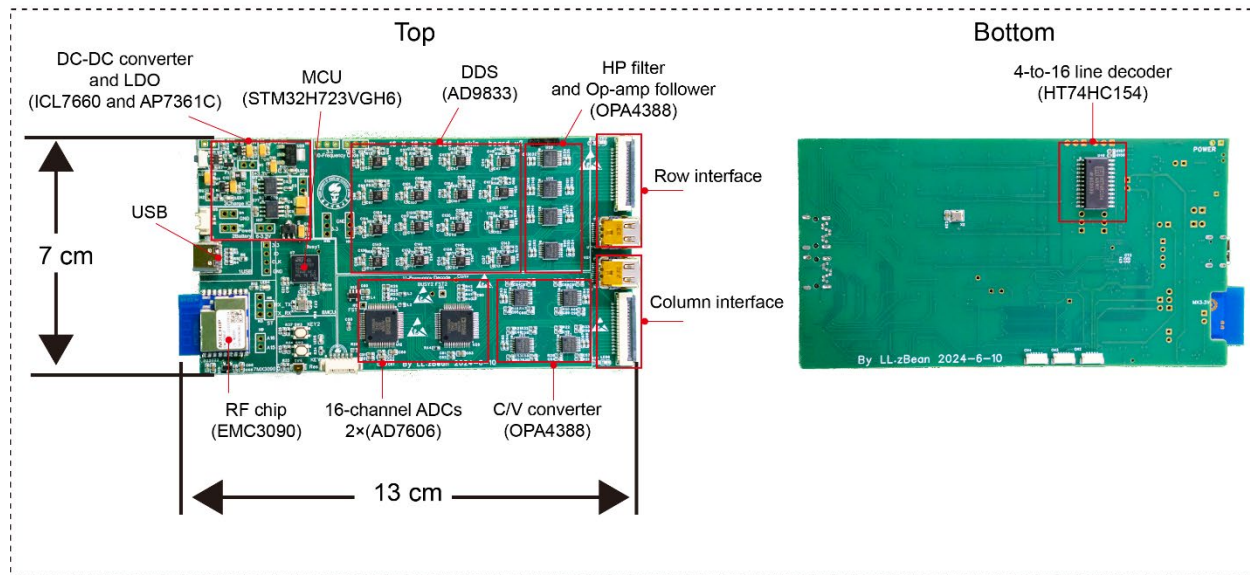
1

2 **Supplementary Figure 14. Mechanism of the frequency-encoding architecture.** Each sensor
 3 unit within the matrix is assigned a unique excitation signal encoded with a distinct sinusoidal
 4 wave frequency. The capacitance response of each sensor correlates with the amplitude of the
 5 corresponding sinusoidal wave. Analog signals from sensor units in each column are aggregated
 6 via a capacitance-to-voltage (C/V converter). A real-time fast Fourier transform (FFT) algorithm
 7 is then applied to decompose the time-domain composite signal, producing a spectral
 8 representation that captures the responses of individual sensor nodes. Finally, the responses of
 9 sensor units at different encoding frequencies are reconstructed into a visual map.
 10

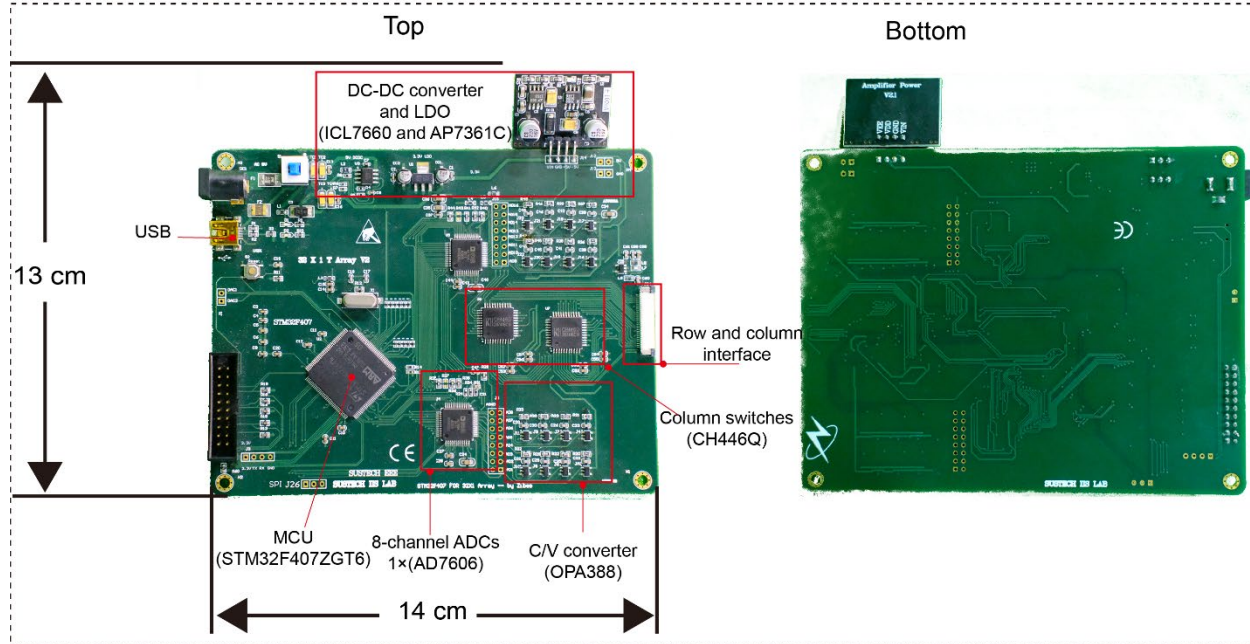


1 **Supplementary Figure 15. Schematic Diagram of Core Components in the Data Acquisition**
2 **Circuit.** This diagram presents an overview of the key modules and components, highlighting the
3 essential functional units of the microcontroller unit (MCU), USB interface, power supply,
4 frequency encoding, analog signal processing and acquisition, analog switch units, and sensor
5 connection interfaces.

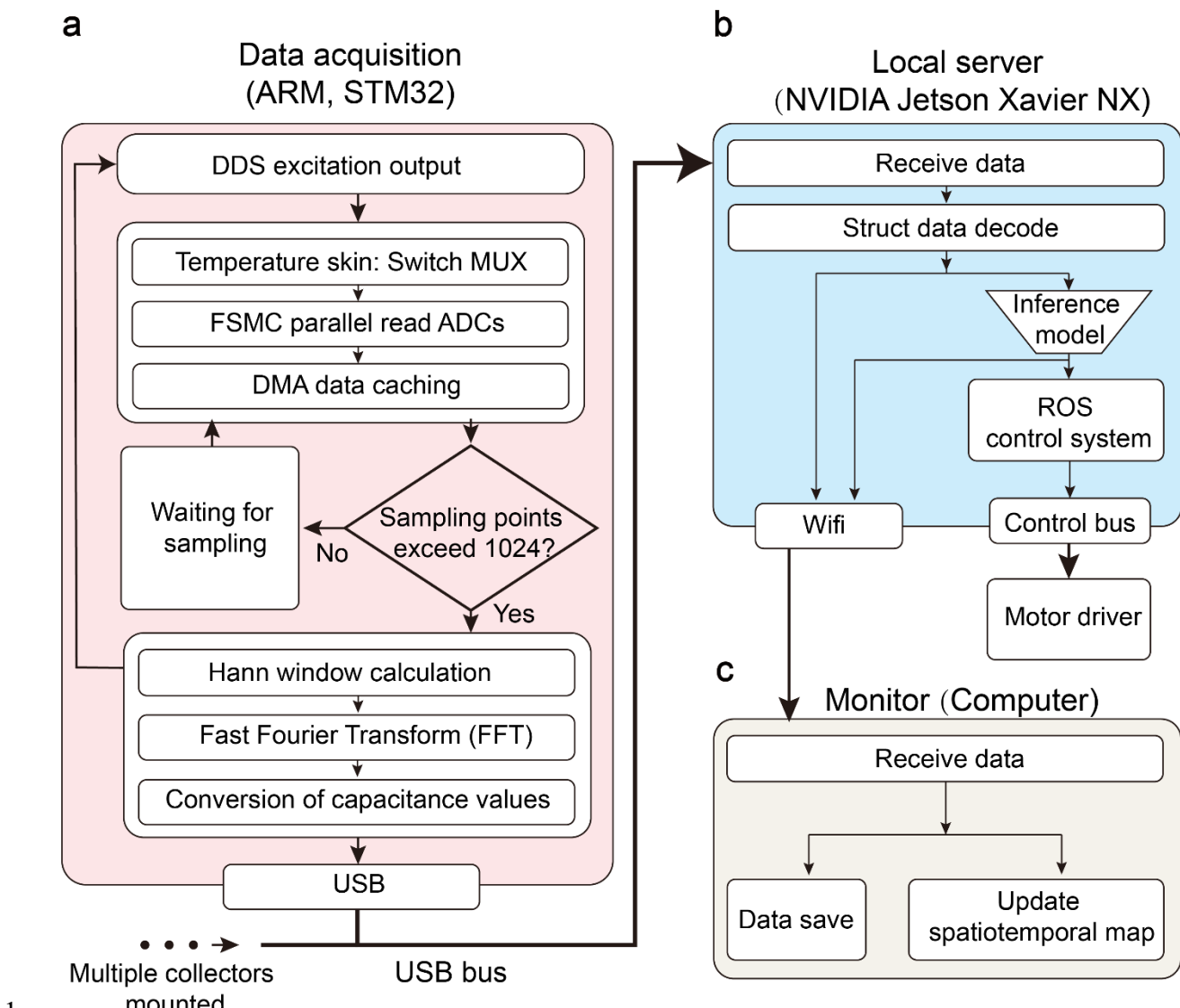
a



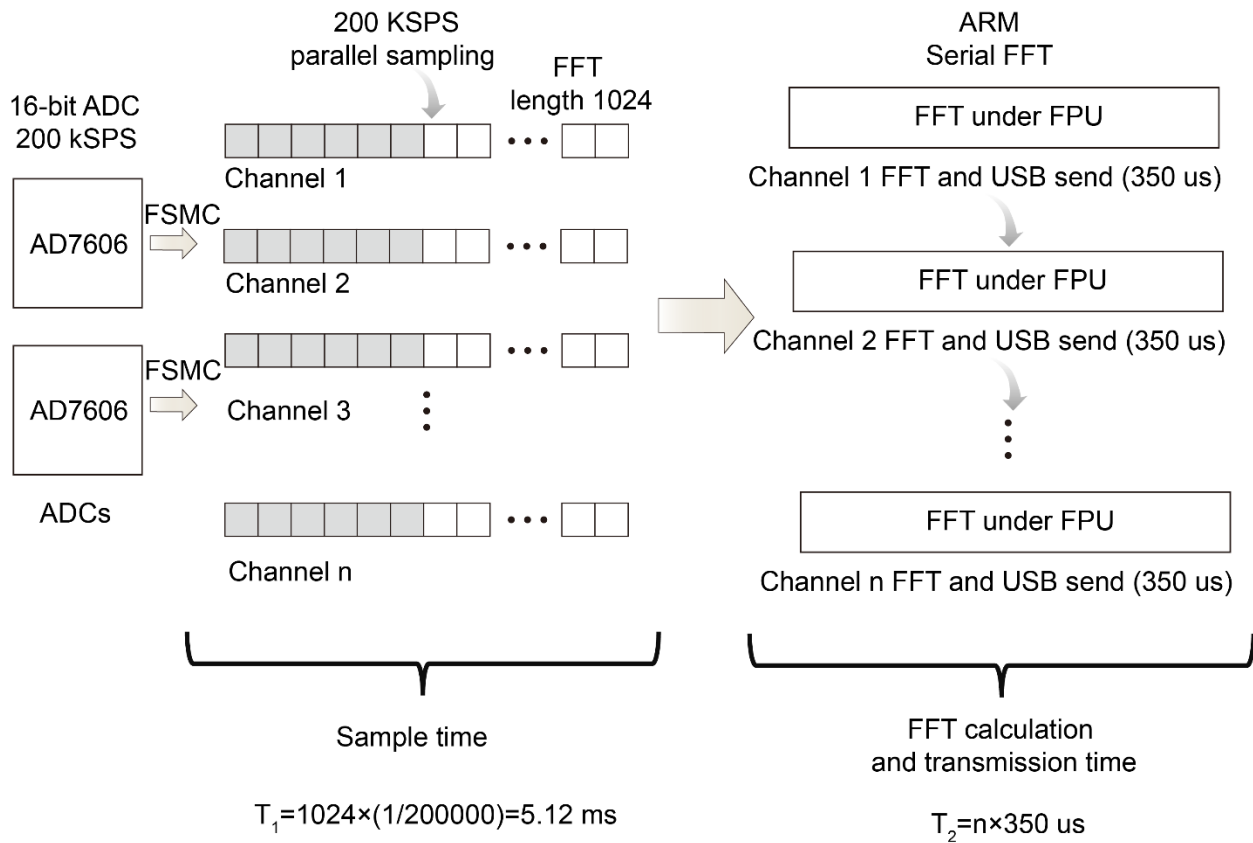
b



2 **Supplementary Figure 16. Physical PCB layout of the data acquisition board.** (a) Printed
3 circuit board (PCB) layout for the pressure skin array acquisition circuit. (b) PCB layout for the
4 temperature skin array acquisition circuit. All chip models and component types are labeled in the
5 diagram.



2 **Supplementary Figure 17. Schematic diagram illustrating the principle and operation of the**
 3 **data acquisition system. (a) Working principle of a data acquisition module. (b) Local server**
 4 **responsible for data collection and parsing. (c) User monitor for data storage and visualization.**

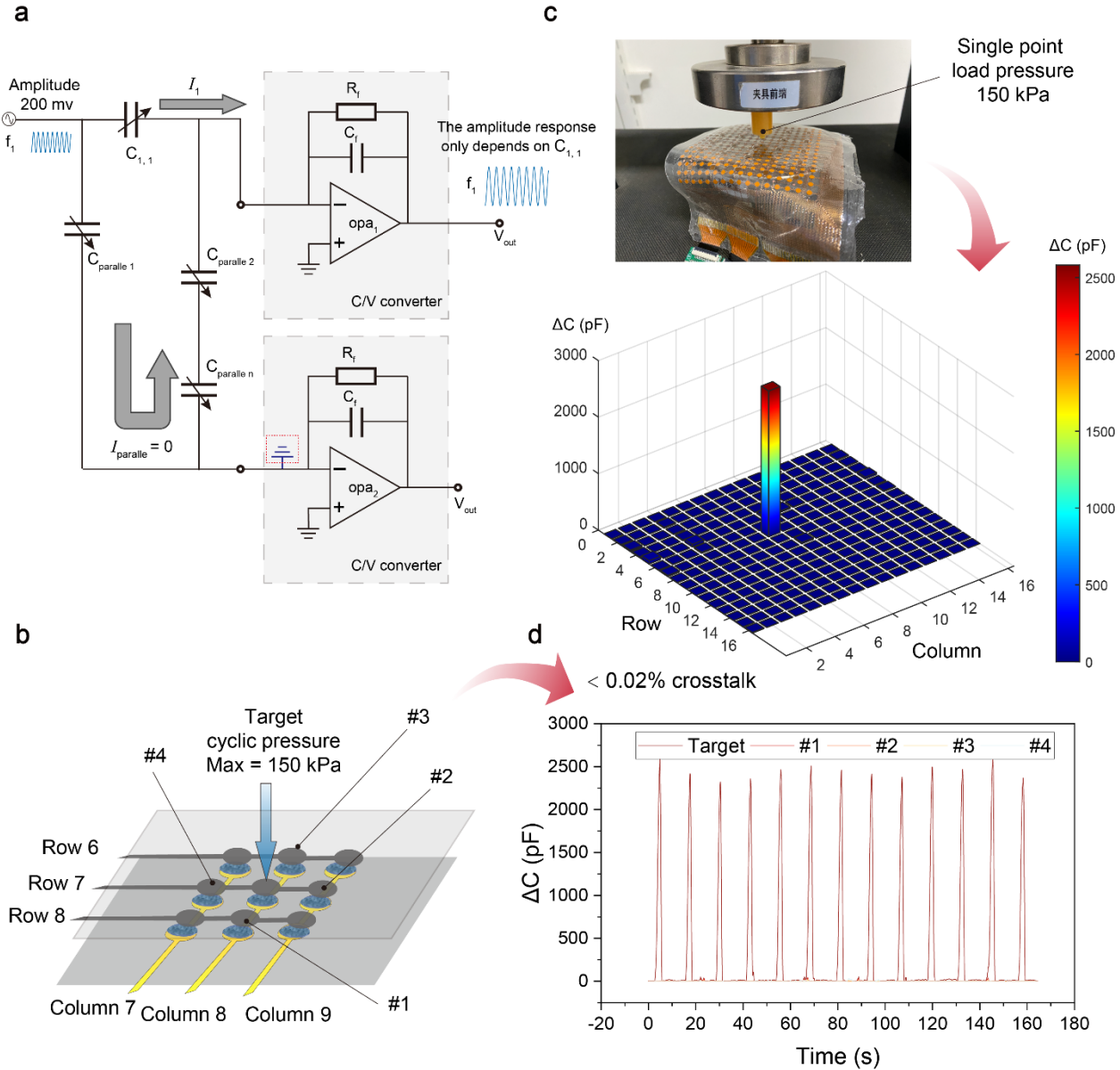


When the sensor is a 16x16 array,
the total time for one frame of data is: $T = T_1 + 16 \times 350 \text{ us} = 10.72 \text{ ms}$

1

Frame rate $\approx 93 \text{ FPS}$

2 **Supplementary Figure 18. Description of the readout circuit frame rate measurement.** The total time expenditure of the measurement circuit is primarily composed of data sampling time and the time required for fast Fourier transform (FFT) computation and data transmission.
3 Abbreviations: FPU, Floating Point Unit; FPS, Frames Per Second.
4
5



1

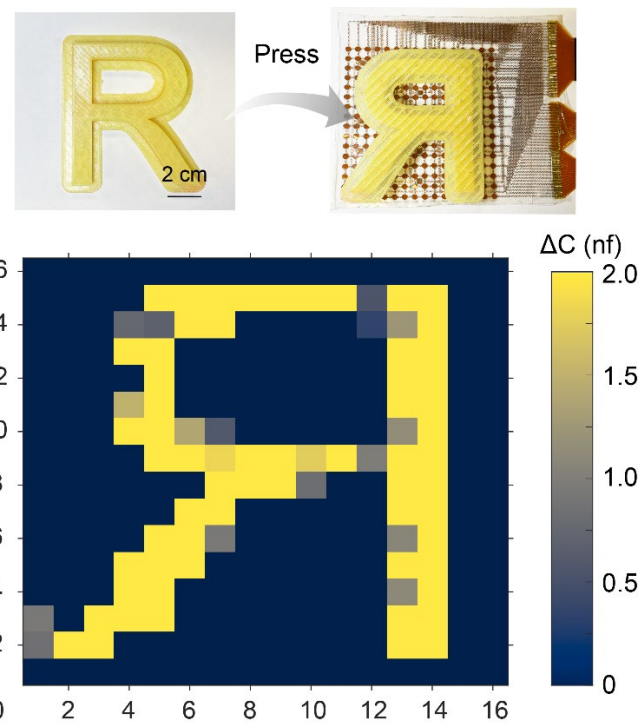
2 **Supplementary Figure 19. Analysis of capacitance crosstalk suppression.** (a) Array circuit
3 structure diagram and local capacitance crosstalk equivalent circuit diagram. The parallel zero-
4 potential mechanism prevents signals from other parallel capacitors from converging². (b)
5 Structure diagram of the isolated microstructured ionic gel design¹, and sensor node labeling. (c)
6 Array signal response map under single-point load of 150 kPa pressure. (d) Under a single point
7 load cyclic pressure of 150 kPa, the crosstalk is <0.02%.

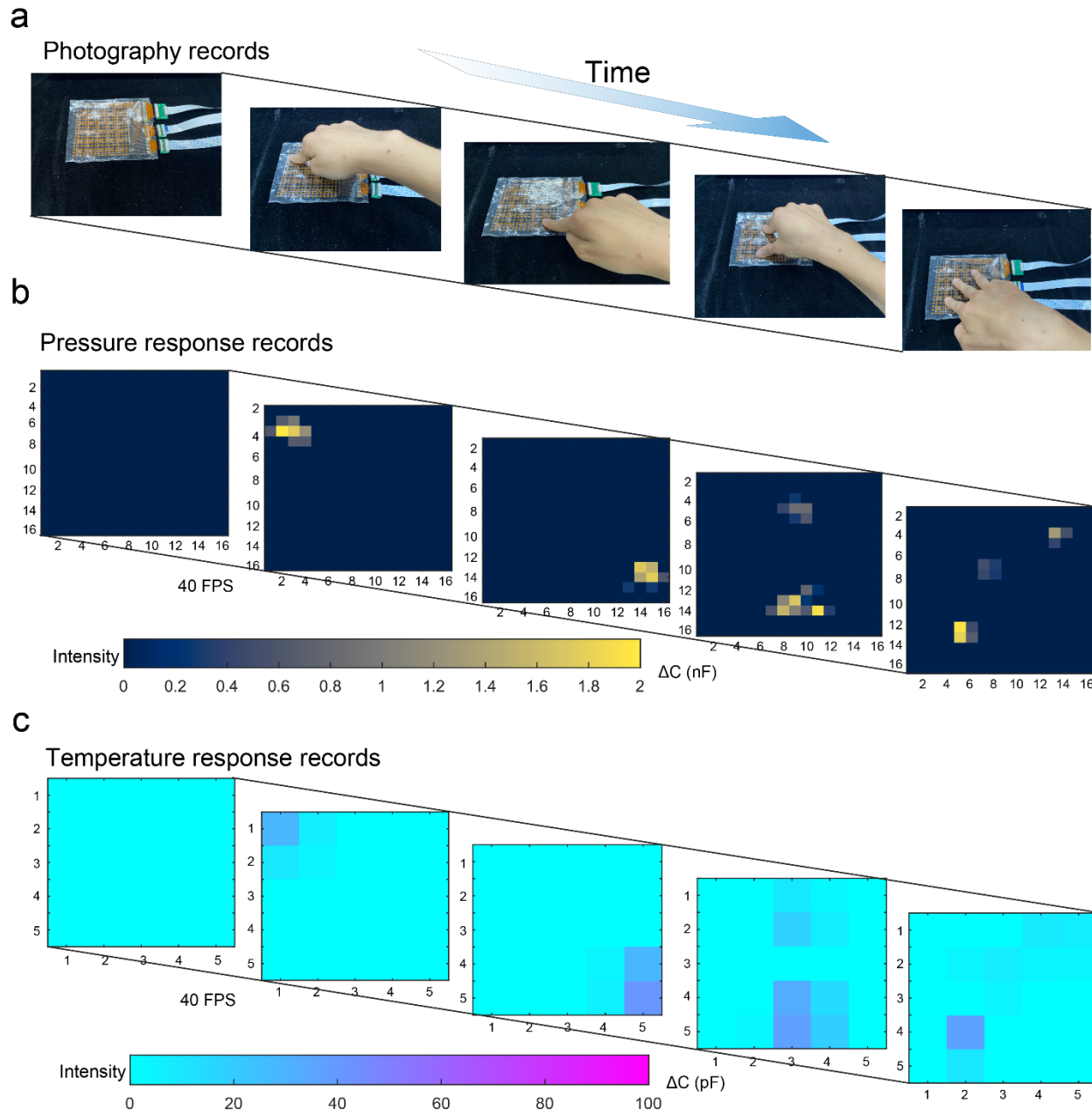
8

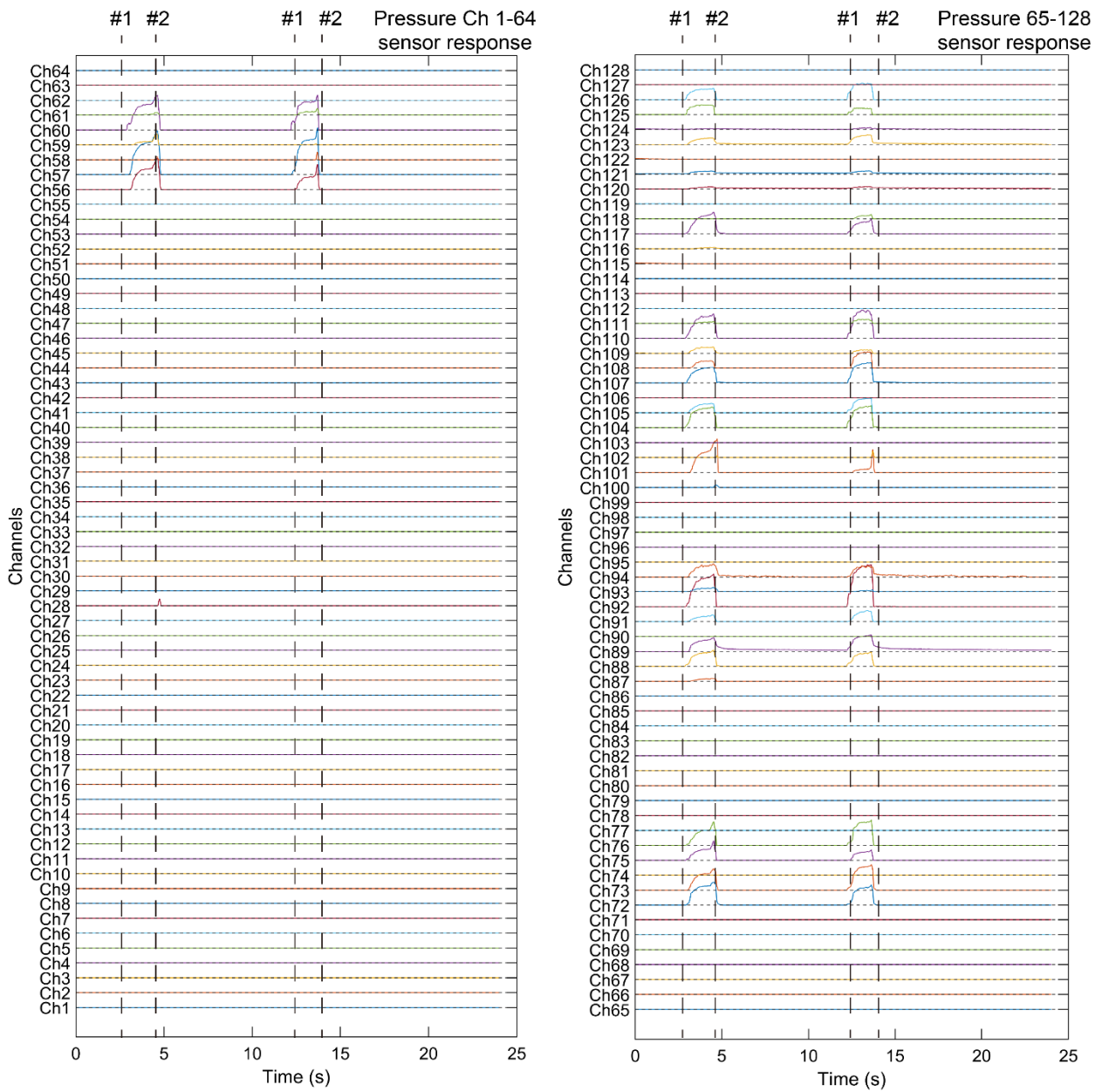
1

2 **Supplementary Figure 20.** The pressure signal mapping of the iontronic skin is acquired
3 under a uniform static pressure of approximately 4 kPa, applied to cover the 3D-printed
4 shape.

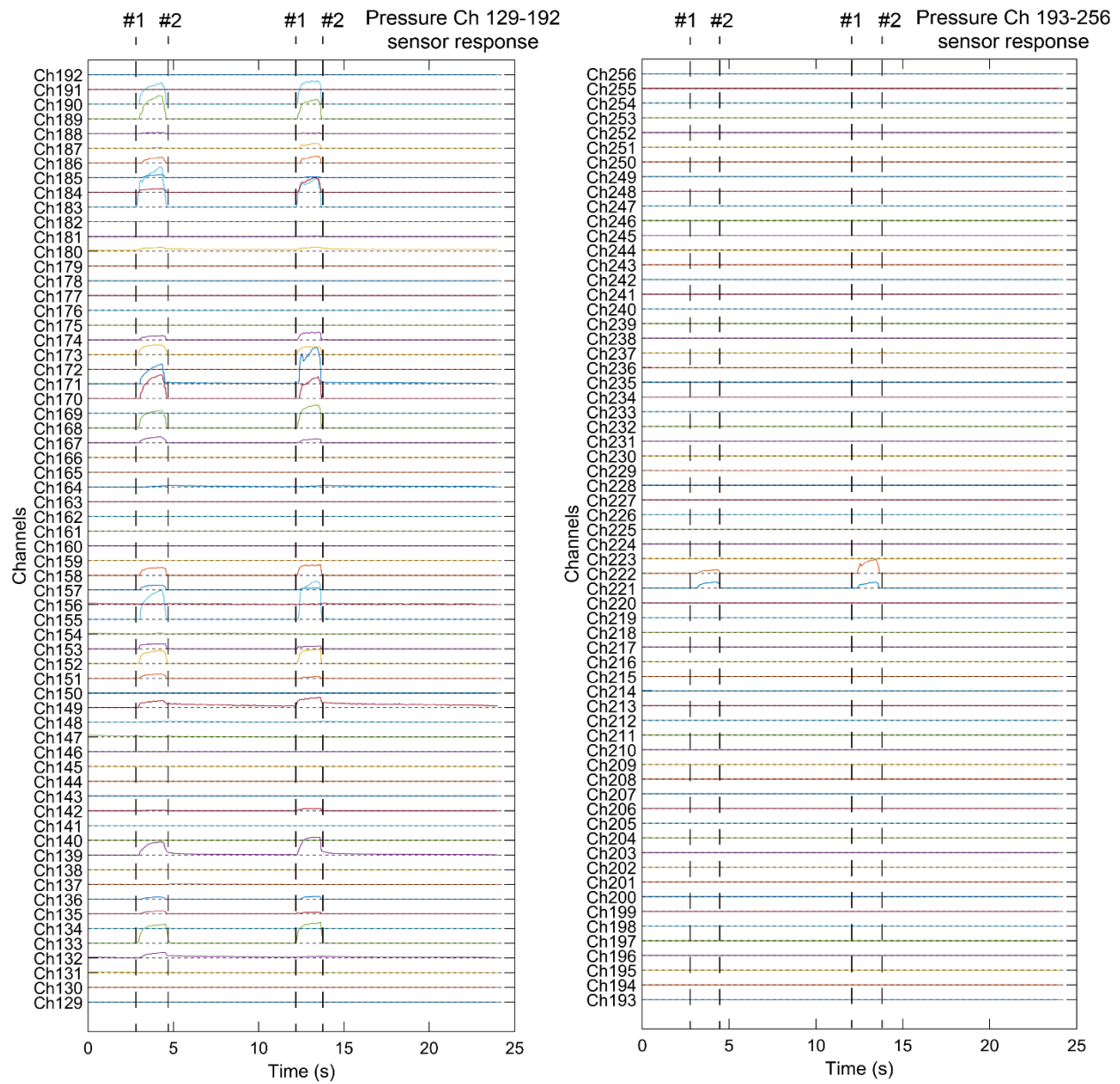
5



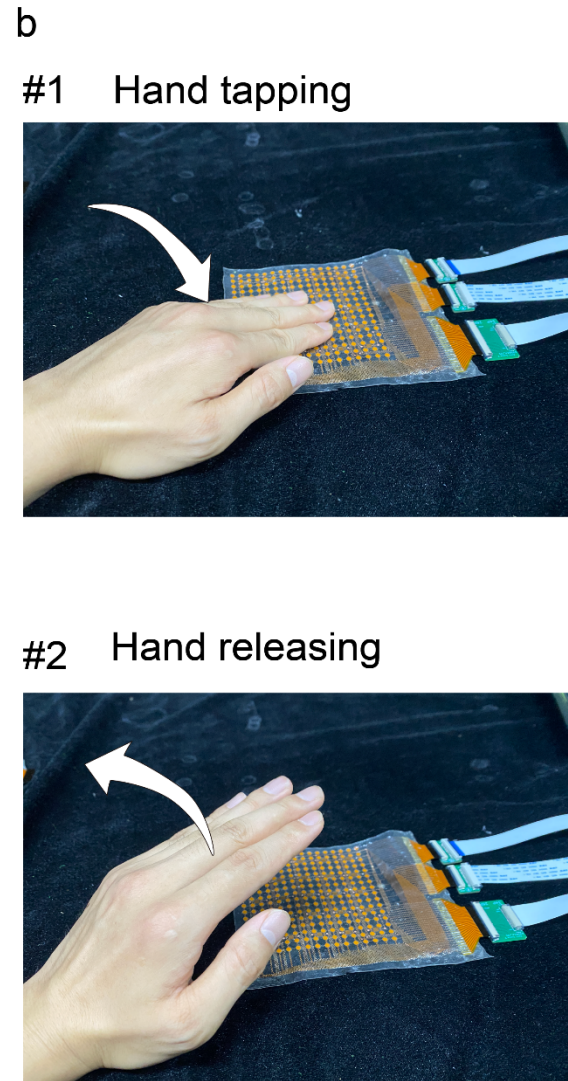
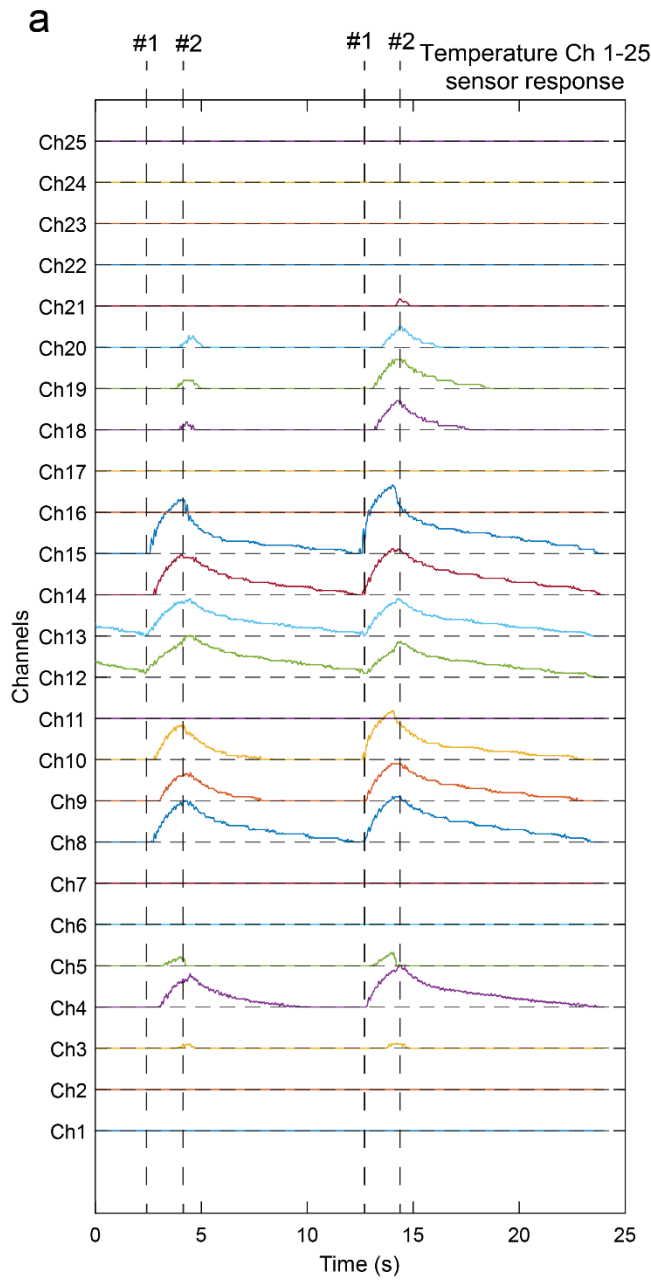




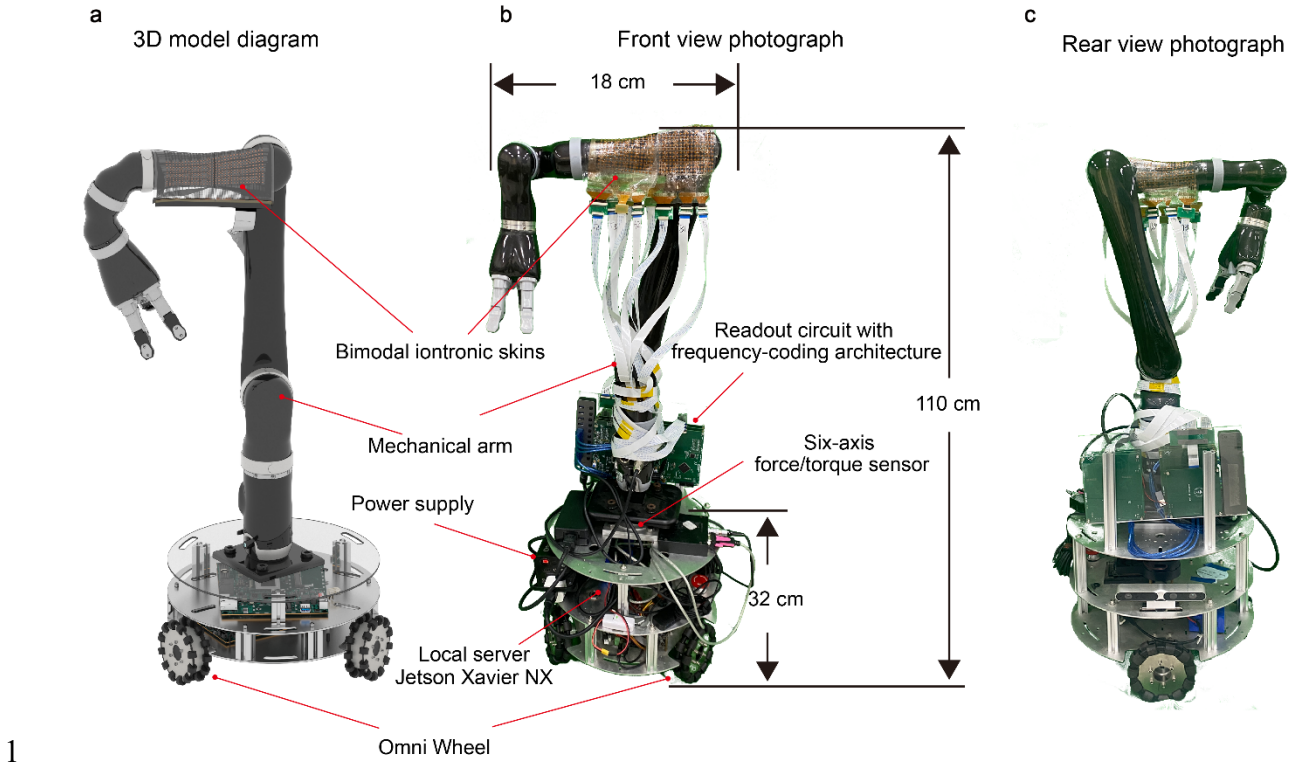
1
2 **Supplementary Figure 22. Pressure time-series responses of channels 1-128 during partial-**
3 **area hand slapping of the sensor array.** #1 indicates the moment the hand makes contact, and
4 #2 indicates the moment the hand is released.
5



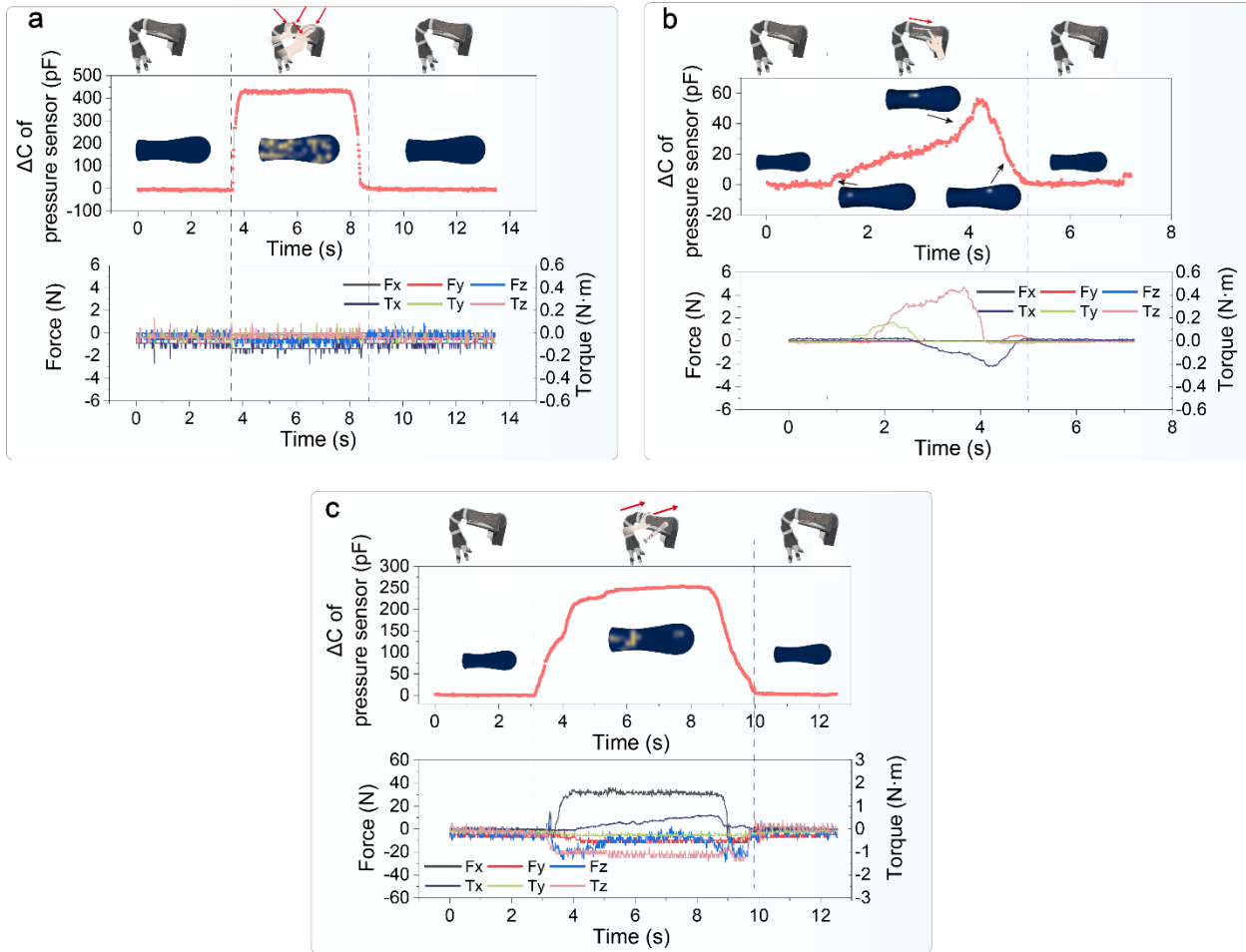
Supplementary Figure 23.1 Pressure time-series responses of channels 129-236 during partial-area hand slapping of the sensor array. #1 indicates the moment the hand makes contact, and #2 indicates the moment the hand is released.



1 **Supplementary Figure 24. Dynamic response recording of the sensor array.** (a) Temperature
2 time-series responses of channels 1-25 during partial-area hand slapping of the sensor array. (b)
3 Description of the hand slapping sensor process. #1 indicates the moment the hand makes contact,
4 and #2 indicates the moment the hand is released.
5

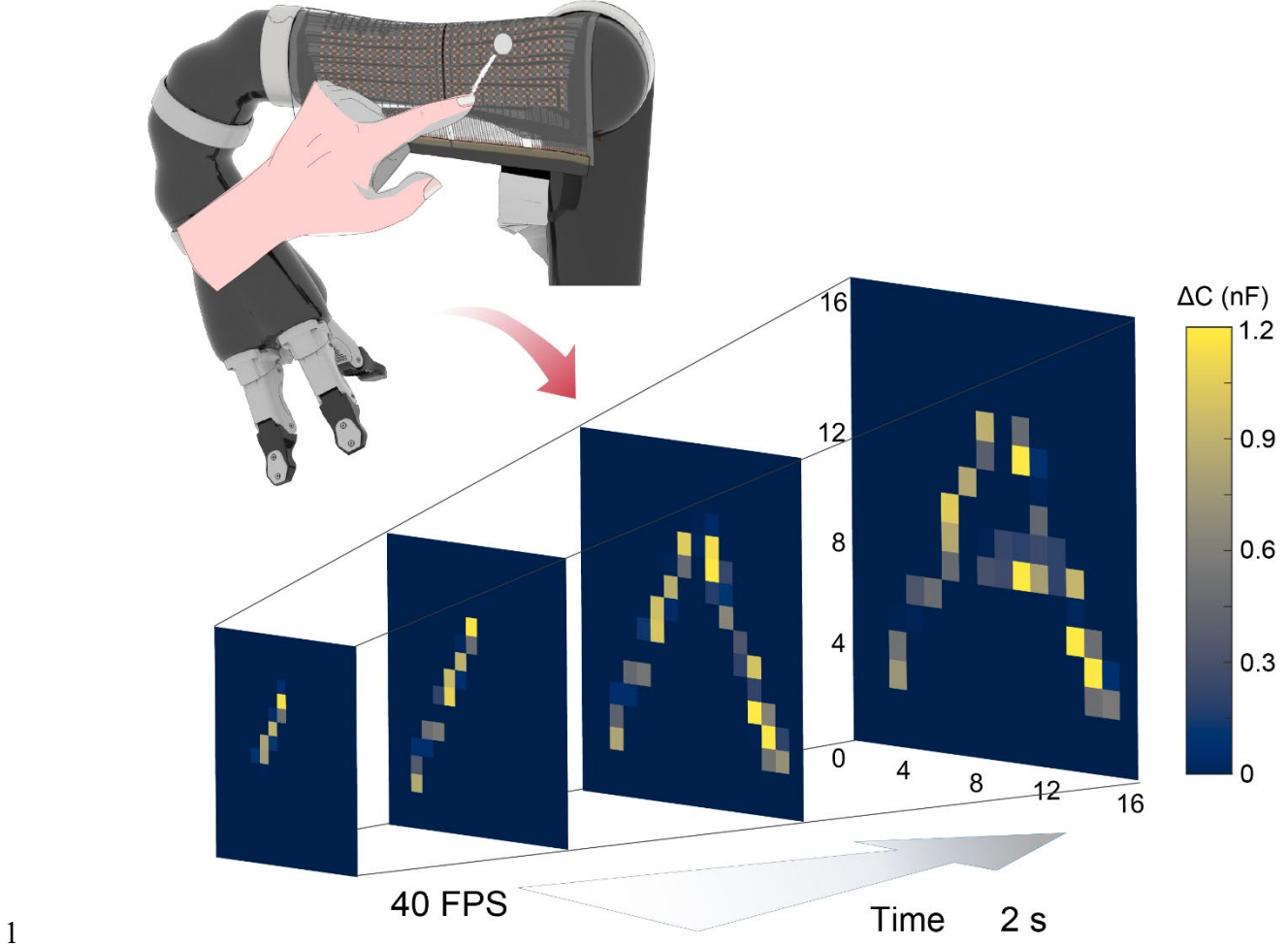


2 **Supplementary Figure 25. Diagram of the collaborative robot's assembly components. (a)**
3 3D model representation. Bimodal iontronic skins are integrated around the forearm section of the
4 robotic arm to facilitate the user's support grip. The base layer comprises a power supply, readout
5 circuit, six-axis force/torque sensor, and a local server. **(b)** Front-view photograph. **(c)** Rear view
6 photograph.



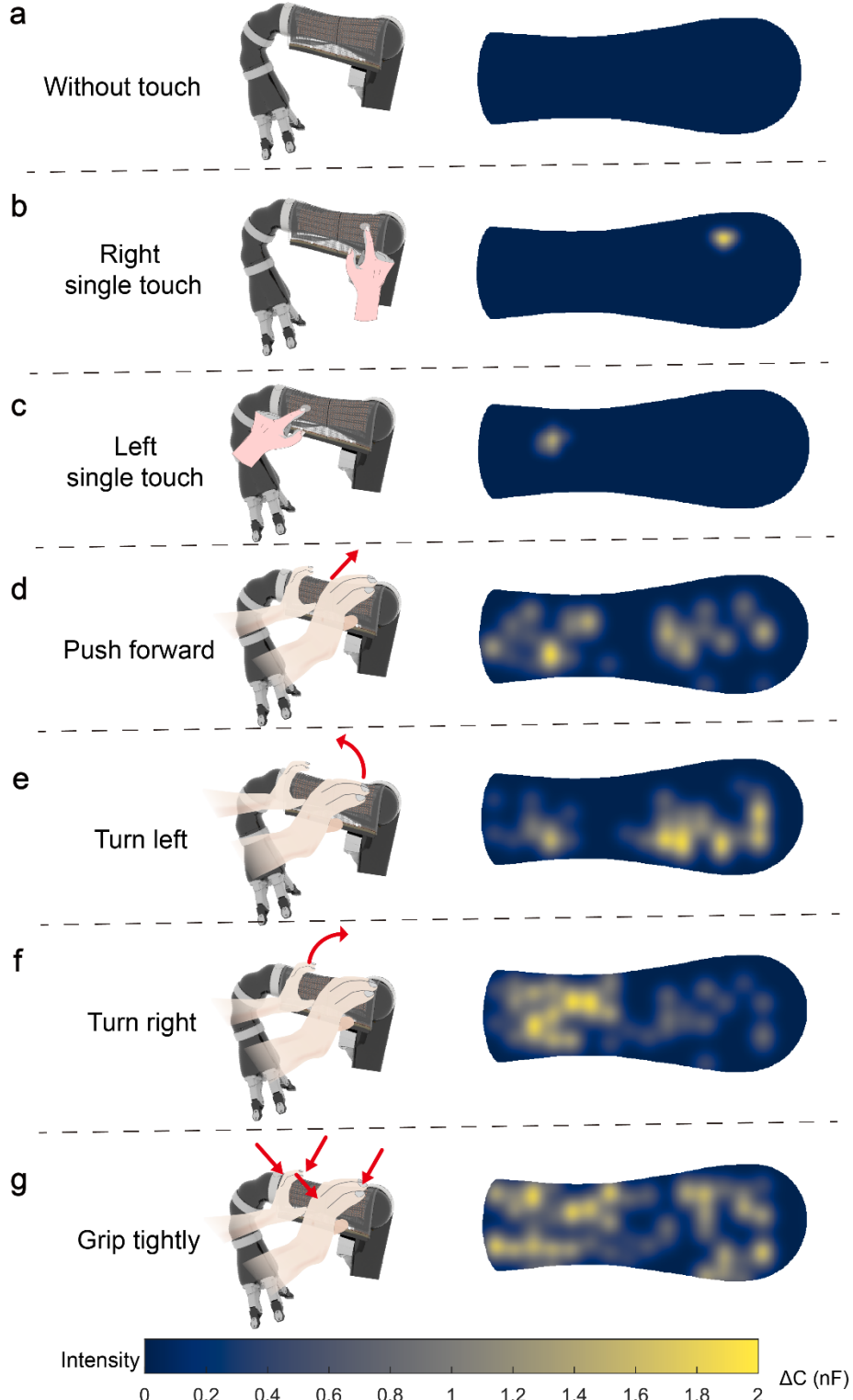
1

2 **Supplementary Figure 26. Comparison of data responses between iontronic skins and six-**
 3 **axis force/torque sensors under different interaction motion modes. (a)** Under gripping force,
 4 the spatial array points on the iontronic skins exhibit a significant response, whereas the six-axis
 5 force/torque sensors show minimal response due to force equilibrium. **(b)** During slight sliding
 6 touch, the iontronic skin array effectively records spatiotemporal signals, while the response from
 7 the six-axis force/torque sensors remains relatively weak. **(c)** Under different object and posture
 8 touches, the iontronic skin array captures distinct spatial features, whereas the six-axis force/torque
 9 sensors struggle to differentiate between various touch patterns.



1

2 **Supplementary Figure 27. Diagram of iontronic skins pressure recording for dynamic touch.**
3 It captures the spatiotemporal pressure variations during the dynamic writing of the letter 'A'.
4

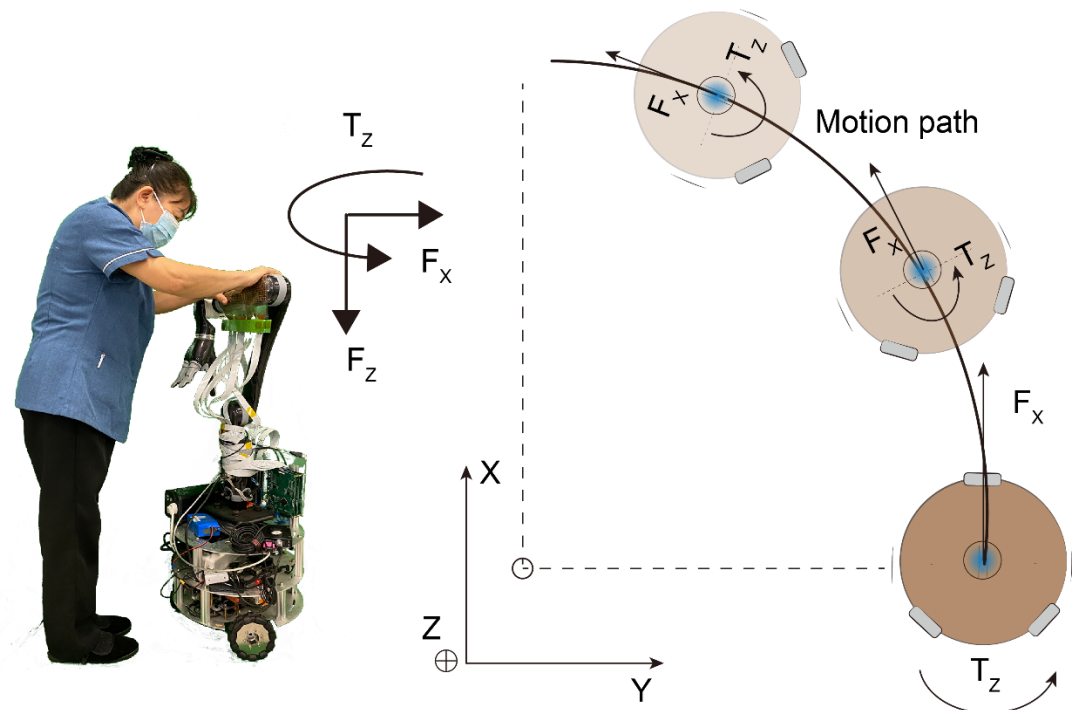


1

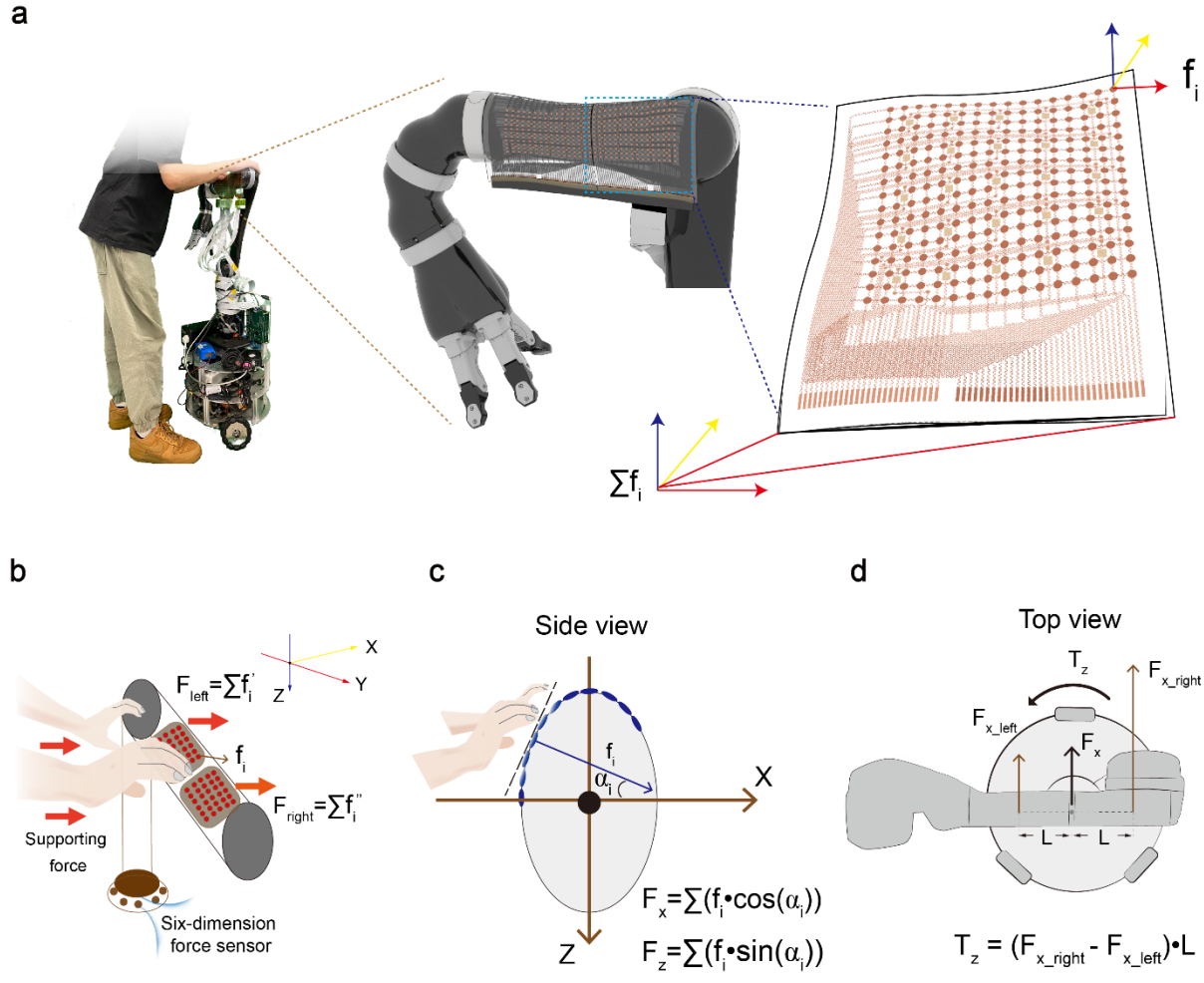
2 **Supplementary Figure 28. Visualization of iontronic skins response under different touch
3 actions.**

4

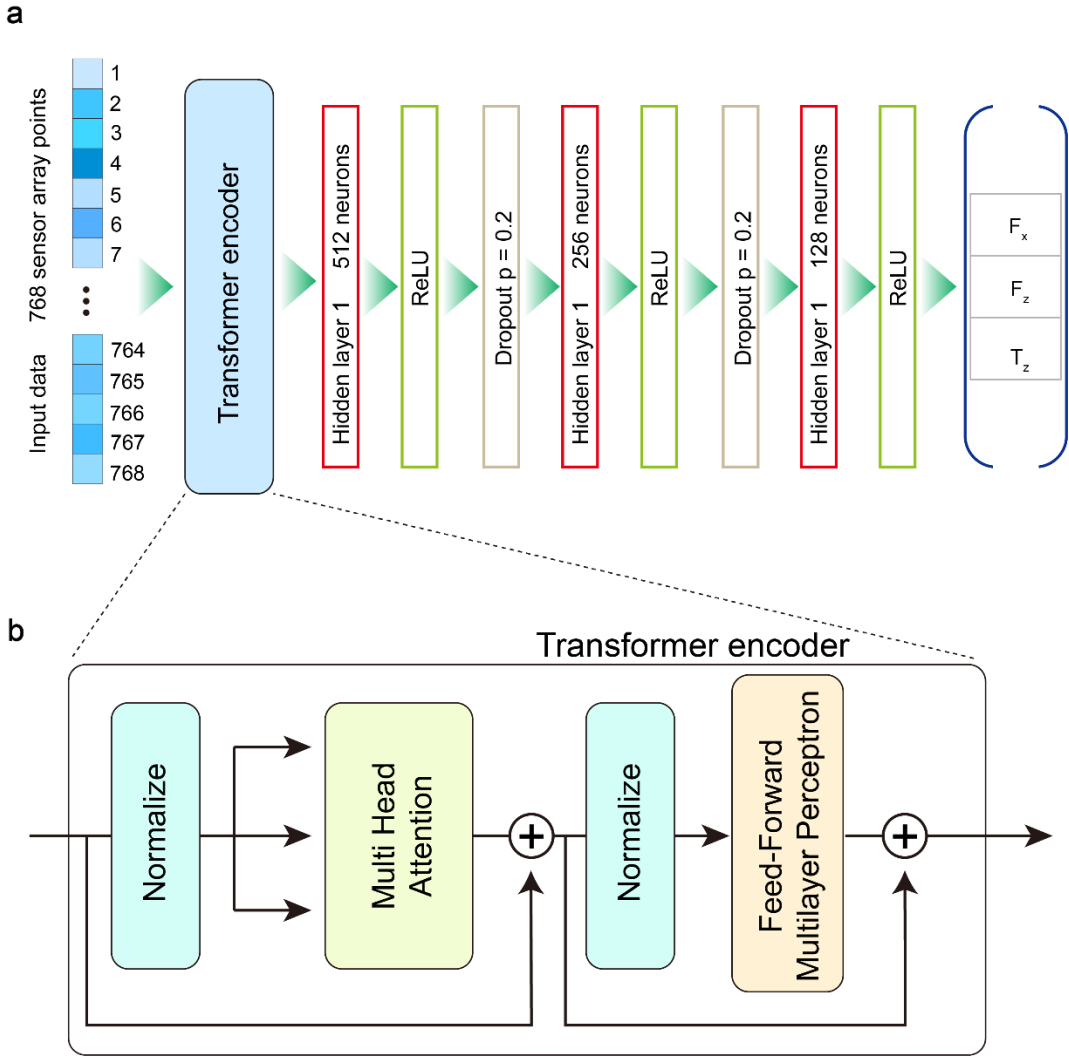
1



2 **Supplementary Figure 29. Explanation of the apparent dynamics model.** The apparent
3 dynamics can be interpreted as the desired dynamics, wherein the robot's walking assistance
4 behavior is guided by the user's intentions.

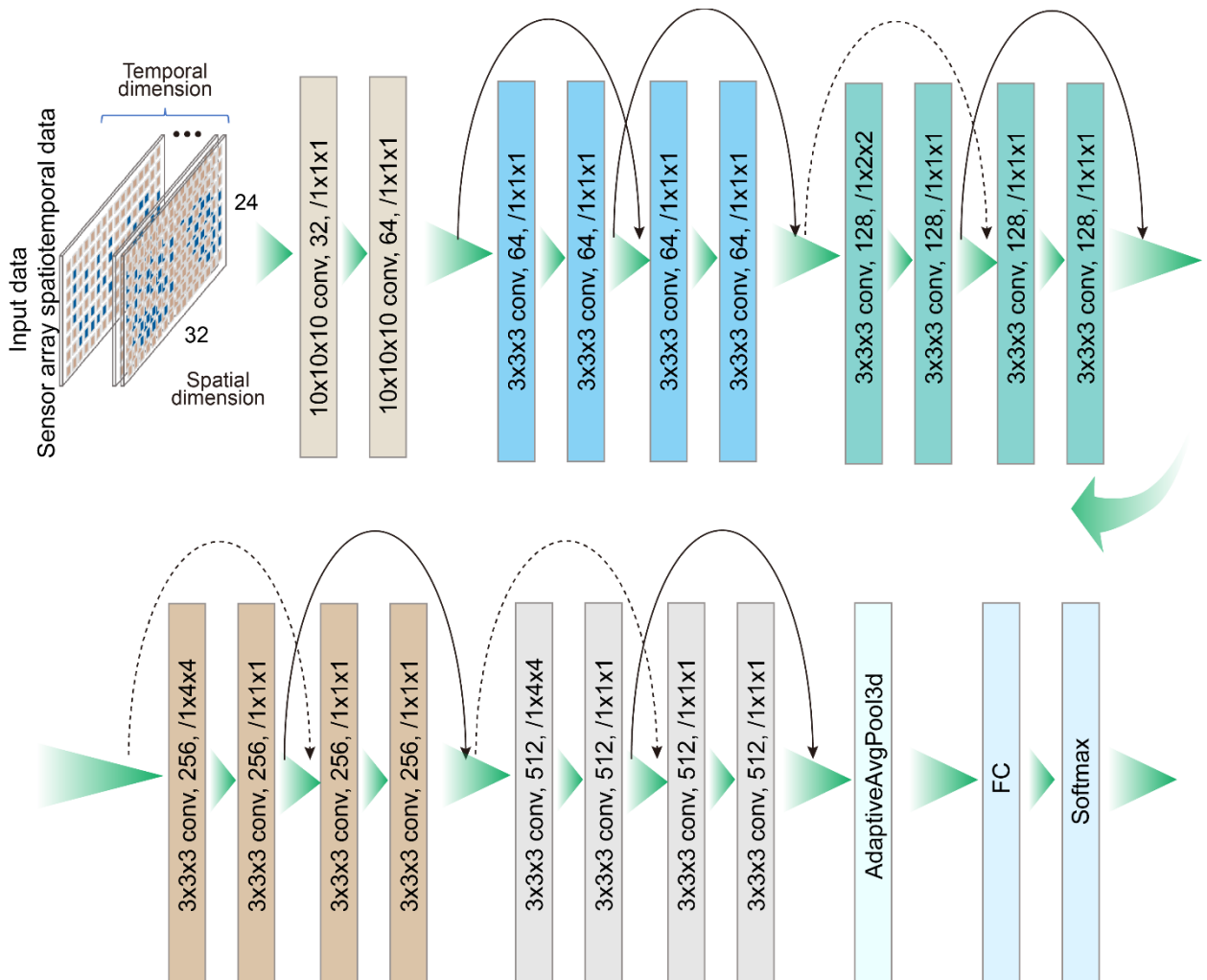


1 **Supplementary Figure 30. Explanation of the vector mechanic model.** (a) Schematic diagram
 2 of our iontronic skins framework. The resultant force on the surface of the flexible sensor is
 3 estimated as the approximate sum of the pressures measured by all the sensor units. (b)
 4 Approximate solution of the resultant force on the left and right handles. (c) Relying on the spatial
 5 positions of the sensor units within the iontronic skins wrapping model to map and decompose the
 6 interaction resultant force. (d) Torque estimation model in the collaborative robot.
 7
 8
 9

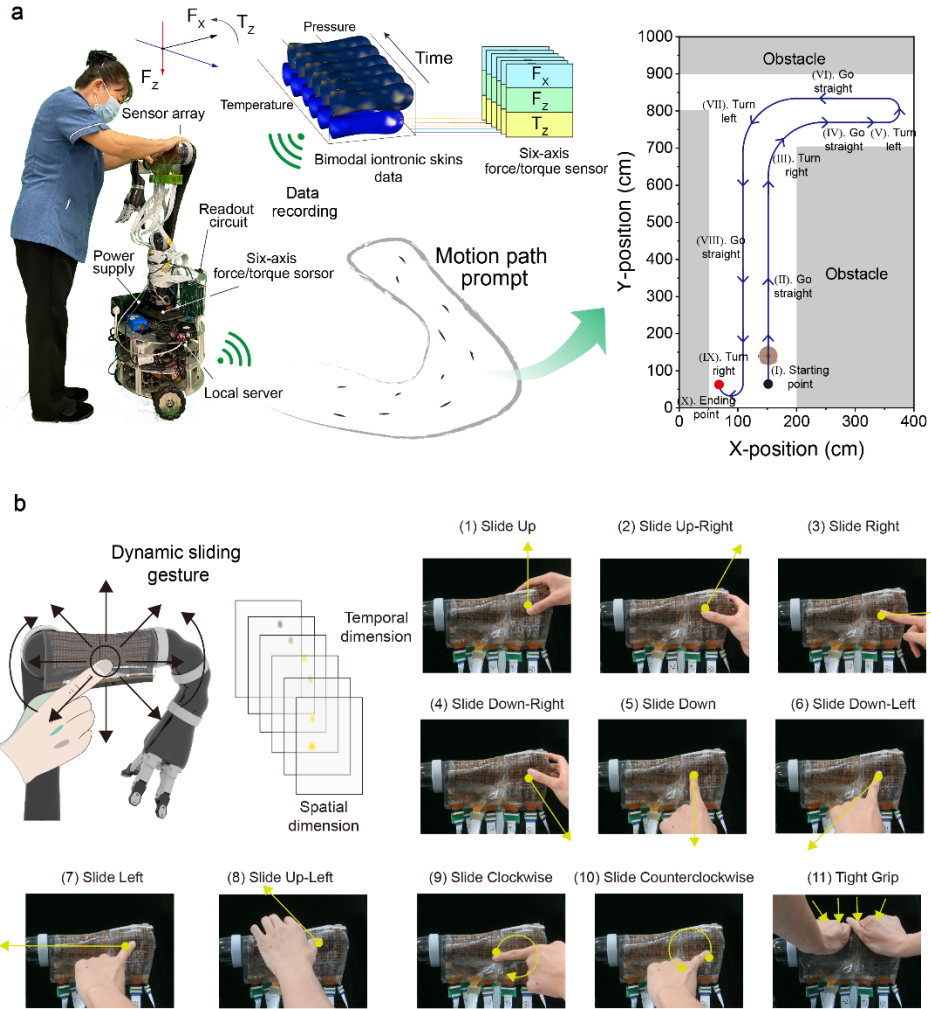


1 **Supplementary Figure 31. Detailed description of the artificial neural network (ANN)**
2 **architecture within the hybrid motion intention model (HMIM).** (a) Schematic representation
3 of the lightweight ANN structure, incorporating the MI-Transformer for learning features from
4 both prior knowledge and real-time data. The MI-Transformer consists of a Transformer encoder
5 and a multilayer perceptron, facilitating accurate inference and prediction of the assisted user's
6 motion intention. This prediction is derived from the distributed somatosensory pressure data
7 captured by the iontronic skins. (b) Detailed architecture of a Transformer encoder block. The
8 input vectors first undergo a multi-head self-attention operation, followed by the first
9 normalization layer, a feed-forward layer, and a second normalization layer. Skip connections, as
10 indicated by the side arrows at the bottom, are incorporated to enhance gradient flow and model
11 stability.

13
14



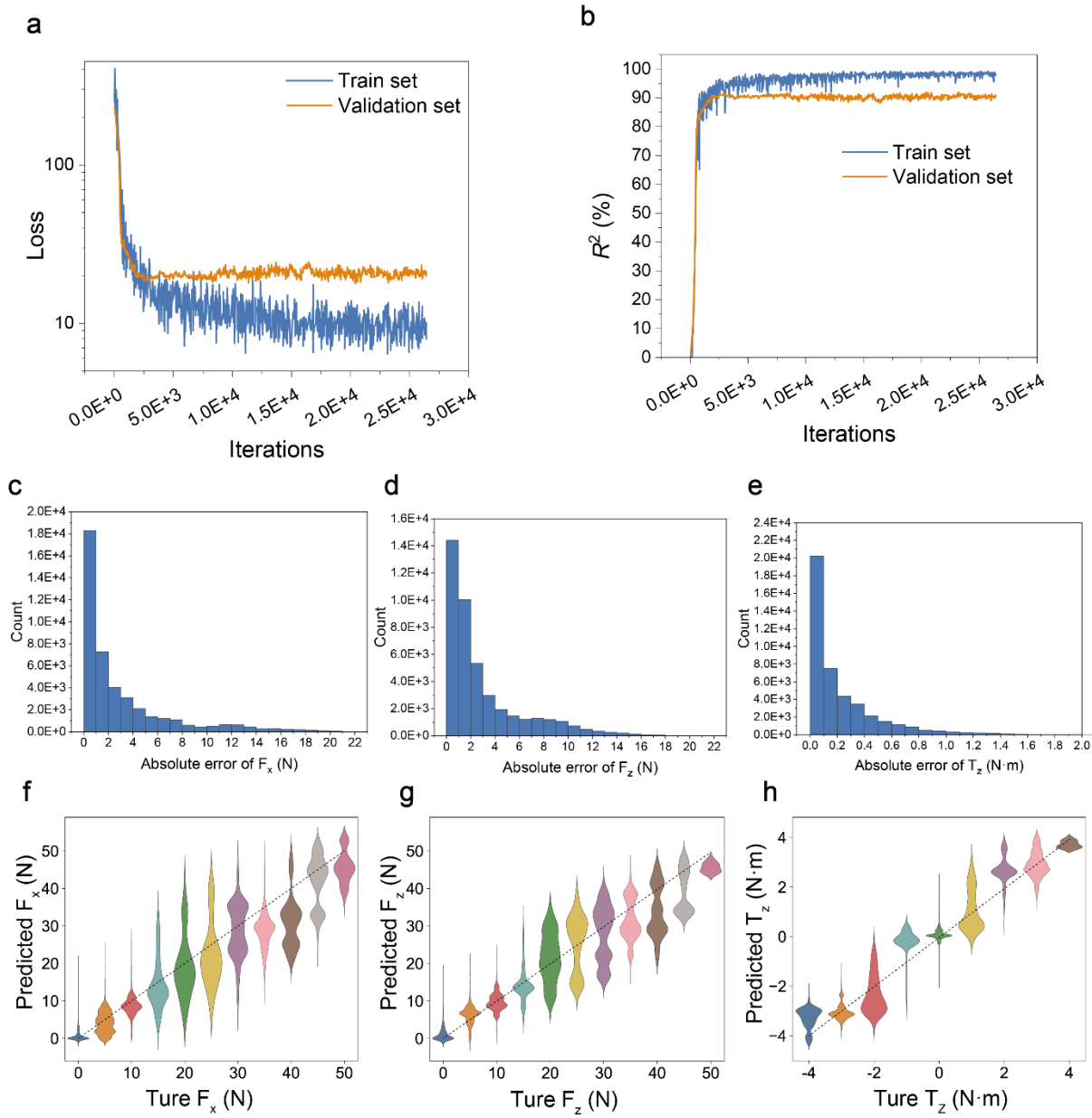
1
2 **Supplementary Figure 32. Res3D architecture.** Downsampling strides are denoted as $t \times w \times h$,
3 where t and $(w \times h)$ are temporal and spatial stride, respectively. Dotted lines are residual
4 connections with downsampling.
5



1

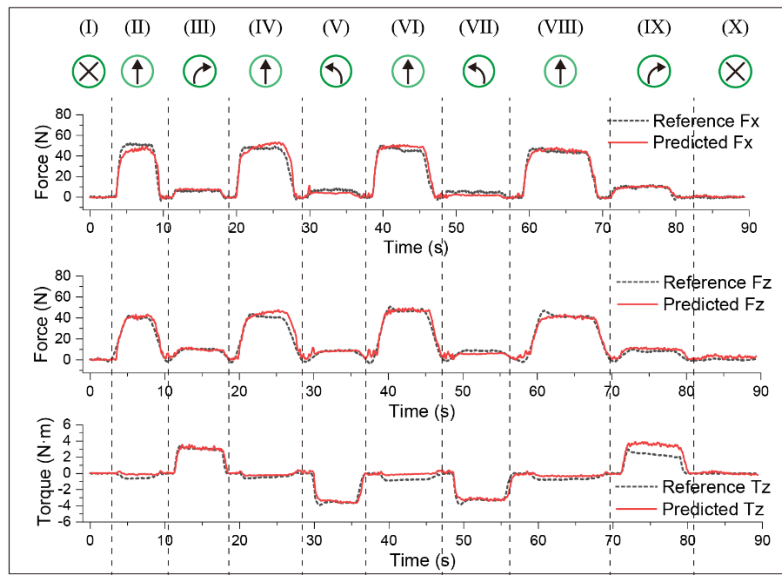
2 **Supplementary Figure 33. Diagram illustrating the process of creating a dataset using**
3 **bimodal iontronic skins. (a)** The MI dataset includes bimodal iontronic skins and six-axis
4 force/torque sensor data (recorded at 40 Hz over more than 200,000 frames) during simulations
5 along various motion paths. The data was collected from 12 participants with different ages and
6 movement habits (ages 20–54, 8 males, 4 females), with each participant completing four rounds
7 of data collection while the robot remained stationary under high damping. In each round,
8 participants simulate their control intentions by applying the expected control force to the robot
9 based on the prompts of the motion path. The data from the iontronic skins is synchronized with
10 the real-time data from the ground truth six-axis force/torque sensor. As shown in the figure on
11 the right, the indicated path styles include different motion states, such as straight movement,
12 large-radius left and right turns, small-radius left and right turns, and stationary states. This data is
13 primarily used to correct the deviation between the iontronic skins data prediction and the six-axis
14 force/torque sensor data. **(b)** The DG dataset comprises dynamic touch data recorded by iontronic
15 skins from 12 participants. These participants performed 11 different dynamic touch gestures,
16 including sliding motions in various directions and firm grips.

17

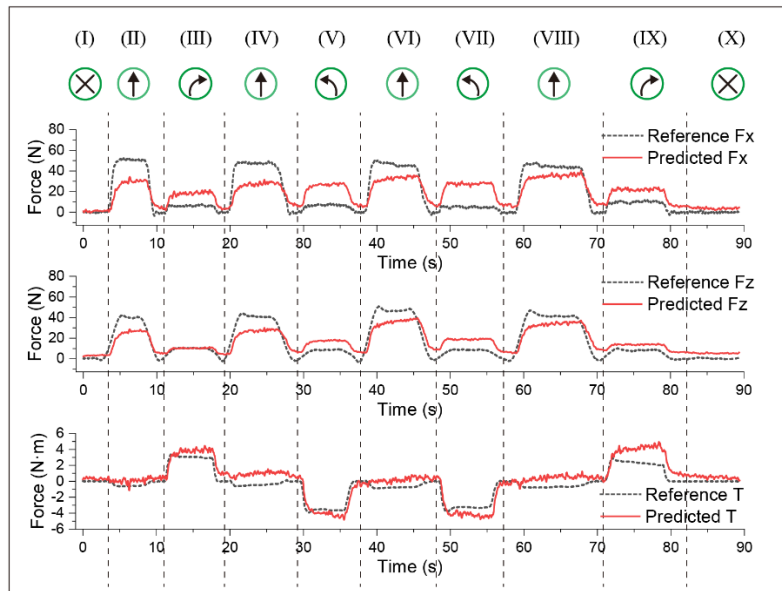


1 **Supplementary Figure 34. Training of the HMIM for the MI prediction base on iontronic**
2 **skins. (a)** Loss convergence curve of the training. **(b)** R^2 convergence curve of the training. **(c)**
3 Statistics of the absolute error of F_x . **(d)** Statistics of the absolute error of F_z . **(e)** Statistics of the
4 absolute error of T_z . **(f to h)** MI inference test results based on the developed HMIM. The test
5 dataset was constructed by experimentally testing samples under different motion intention paths
6 from two subjects.

a

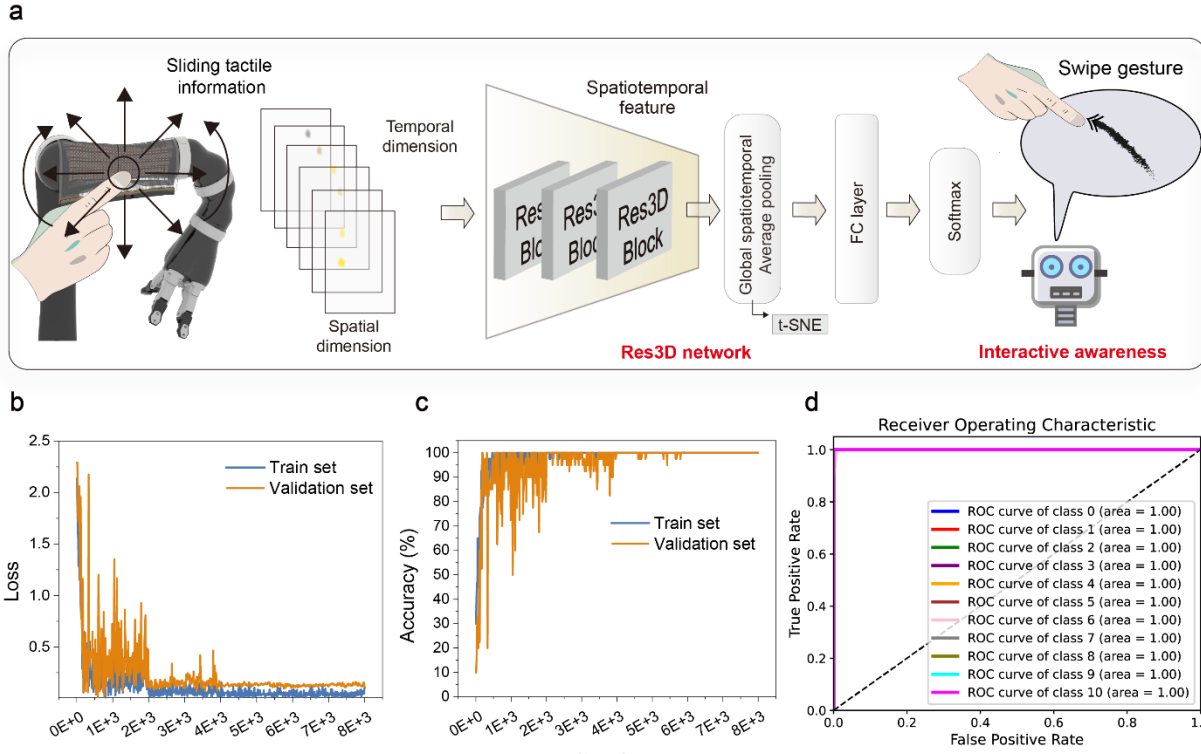


b



1

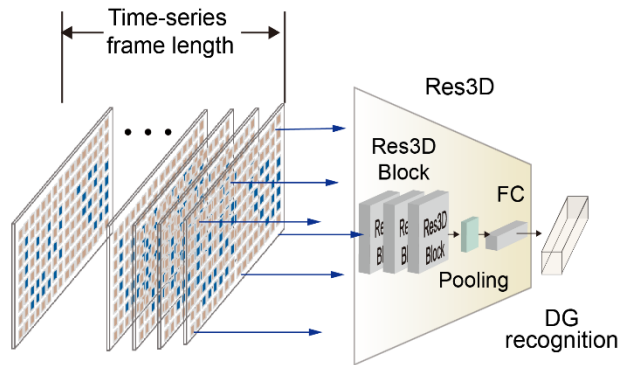
2 **Supplementary Figure 35.** (a) Comparison of MI inference results with the ground truth reference
 3 over a complete motion cycle during the HMIM inference testing. (b) Comparison of MI inference
 4 results with the ground truth reference over a complete motion cycle during the physical model
 5 VMM inference testing. The prediction of the physical model deviates from the actual ground truth
 6 due to sensor attachment errors and consistency errors in the sensing units.
 7



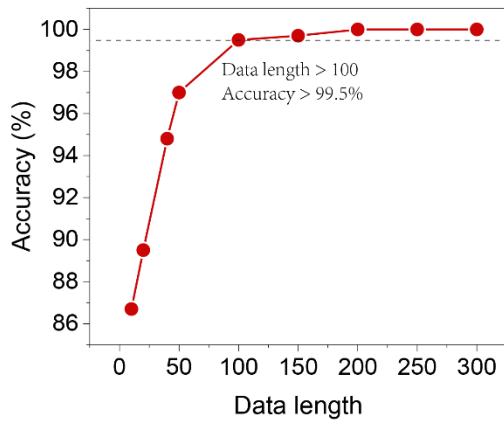
1

2 **Supplementary Figure 36. Training of the DG recognition Res3D based on iontronic skins**
3 **(Time frame length=100).** (a) Res3D network recognition process diagram. (b) Loss convergence
4 curve of the training. (c) Accuracy convergence curve of the training. (d) The Receiver Operating
5 Characteristic (ROC) curves of the Res3D network for recognizing 11 types of dynamic touch
6 gestures based on iontronic skins.

7

1
a

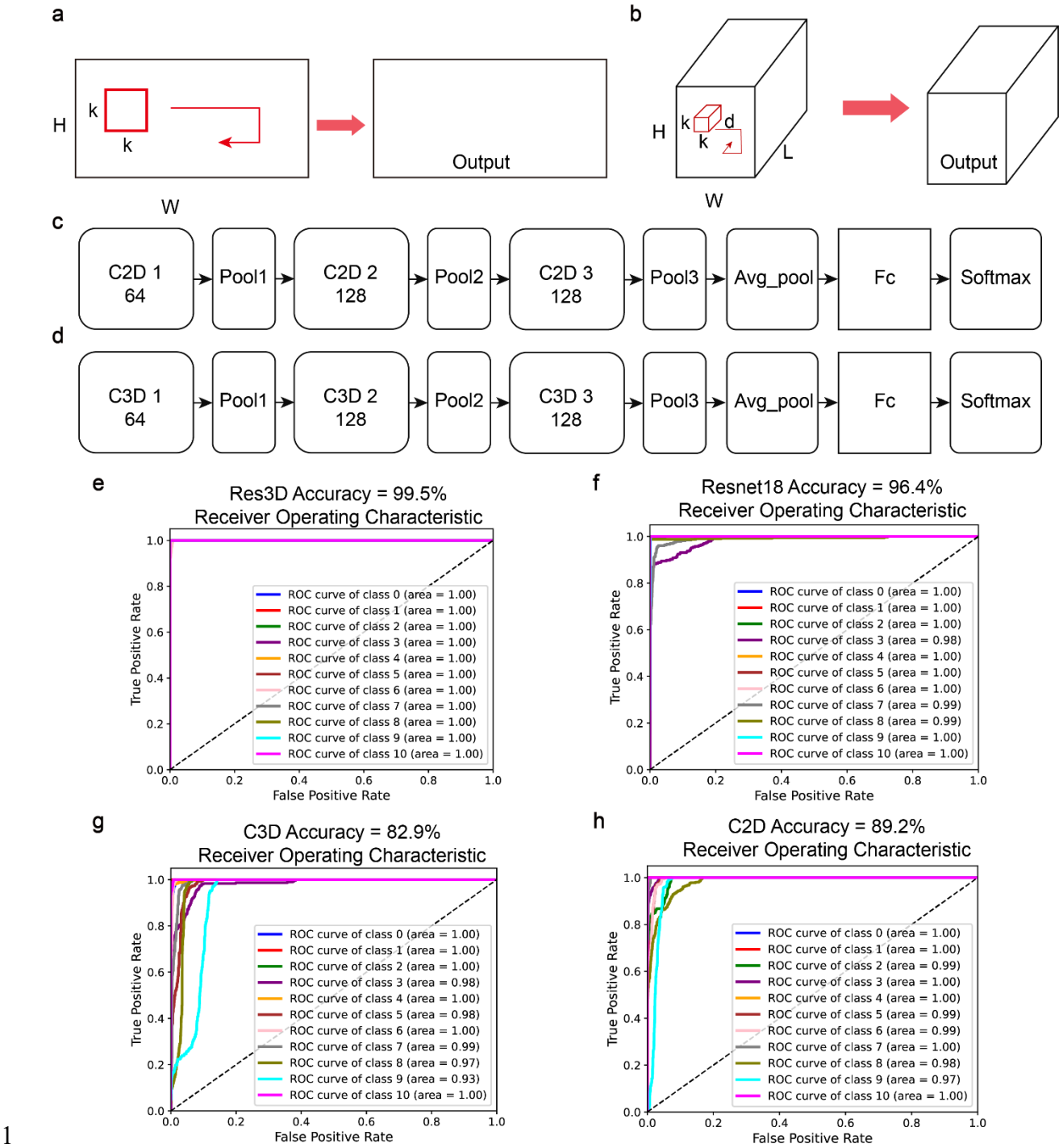
b



1

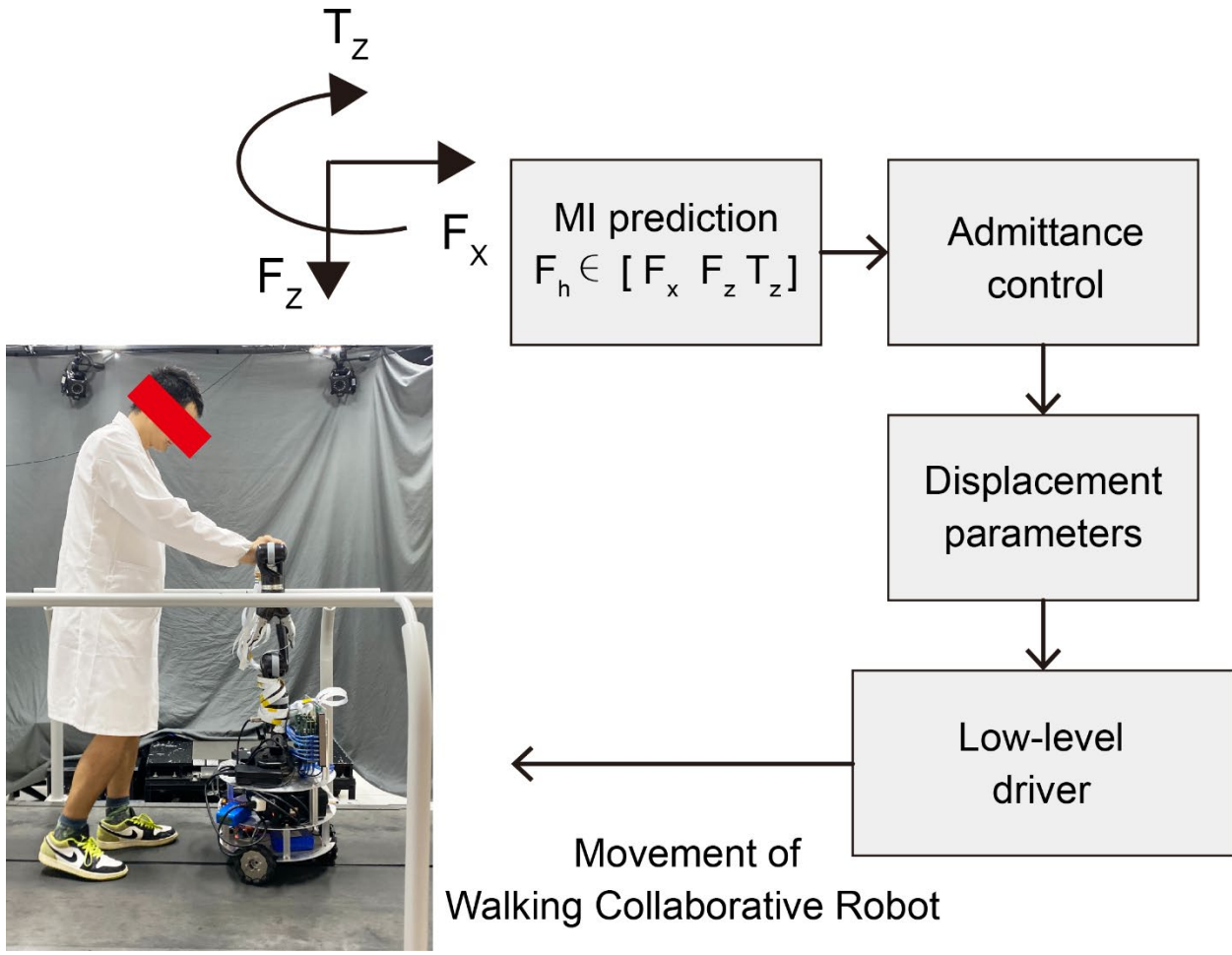
2 **Supplementary Figure 37. Experiment on the impact of temporal frame lengths on**
3 **recognition accuracy. (a)** The recognition process across varying temporal frame lengths. **(b)**
4 Recognition accuracy corresponding to different temporal frame lengths.

5

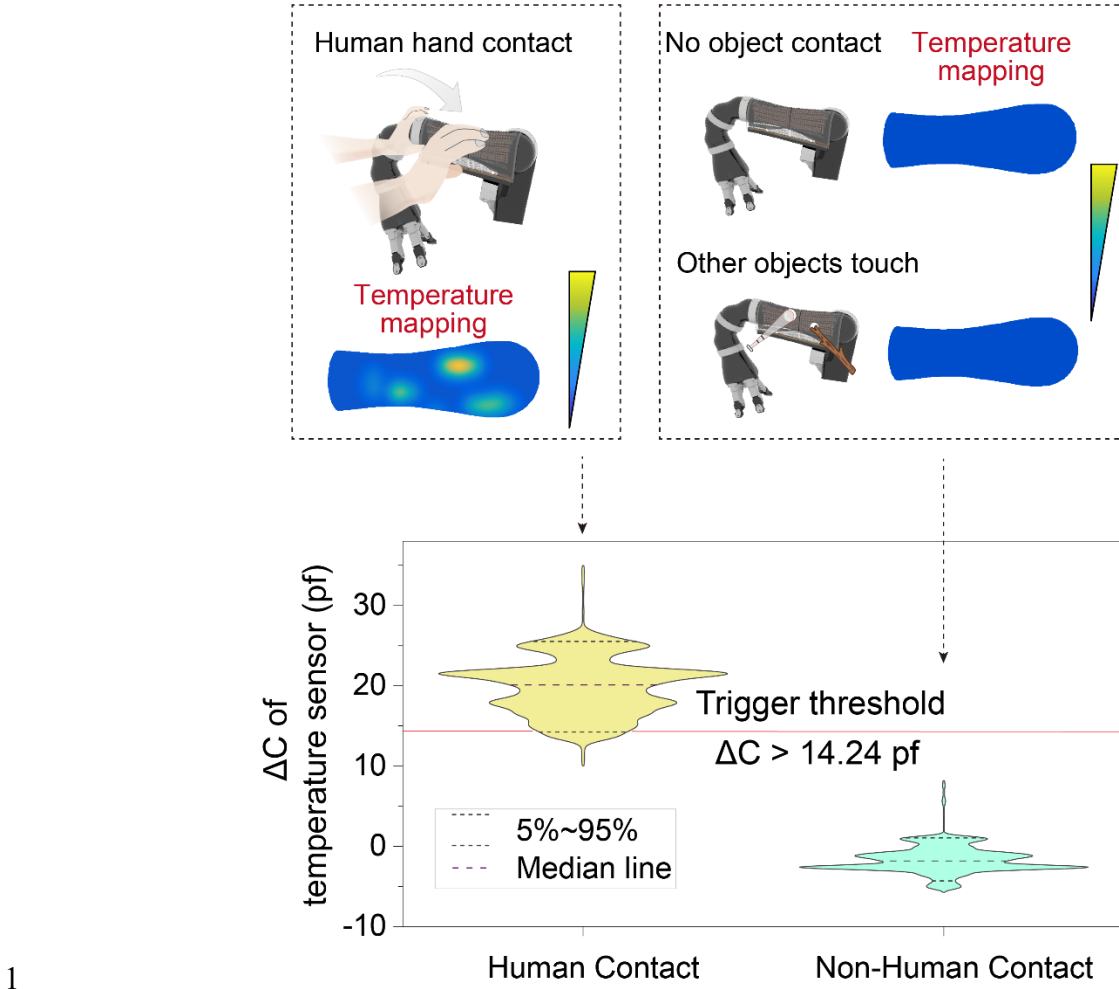


1 **Supplementary Figure 38. Comparison of recognition performance of different mainstream**
2 **neural networks on dynamic somatosensory time-series data.** (a) 2D convolution architecture¹³.
3 Applying 2D convolution on a touch data volume (multiple frames flattened as one plane) also
4 results in an image. (b) 3D convolution architecture¹⁴. Applying 3D convolution on a data volume
5 results in another volume, preserving spatiotemporal information of the input signal. (c) The 2D
6 Convolutional Neural Network (C2D) consists of three 2D convolution layers, three max-pooling
7 layers, an adaptive average pooling layer, and a fully connected layer, followed by a softmax
8 layer.

1 output layer. **(d)** The 2D Convolutional Neural Network (C3D) consists of three 3D convolution
2 layers, three max-pooling layers, an adaptive average pooling layer, and a fully connected layer,
3 followed by a softmax output layer. **(e)-(h)** Receiver Operating Characteristic (ROC) curves for
4 Res3D, ResNet18, C3D, and C2D in recognizing 11 types of dynamic touch gestures. Res3D
5 demonstrates superior spatiotemporal feature extraction and higher accuracy in gesture recognition.
6



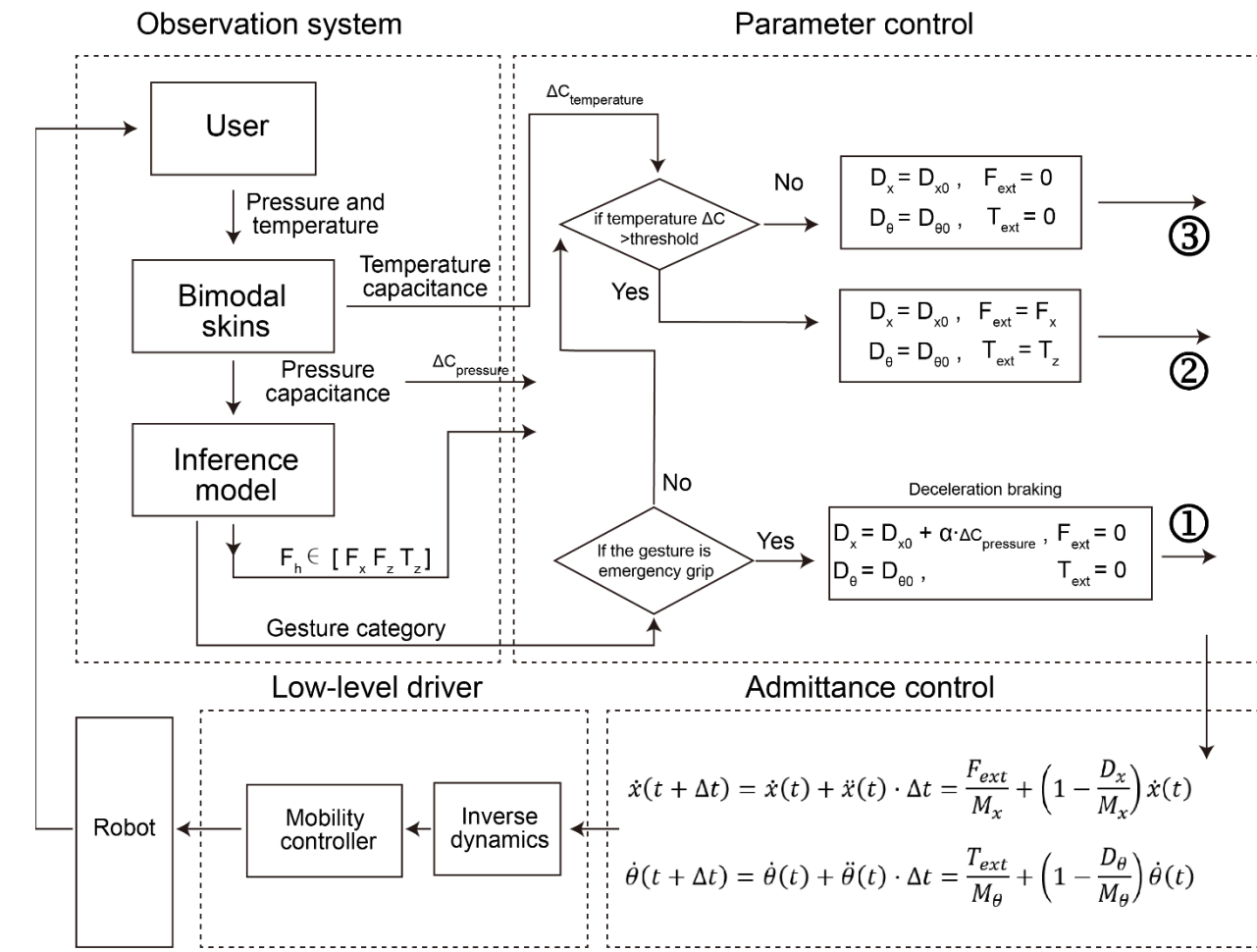
2 **Supplementary Figure 39. Motion control diagram for a robot-assisted walking system**
 3 **implementing passive behavior.**
 4



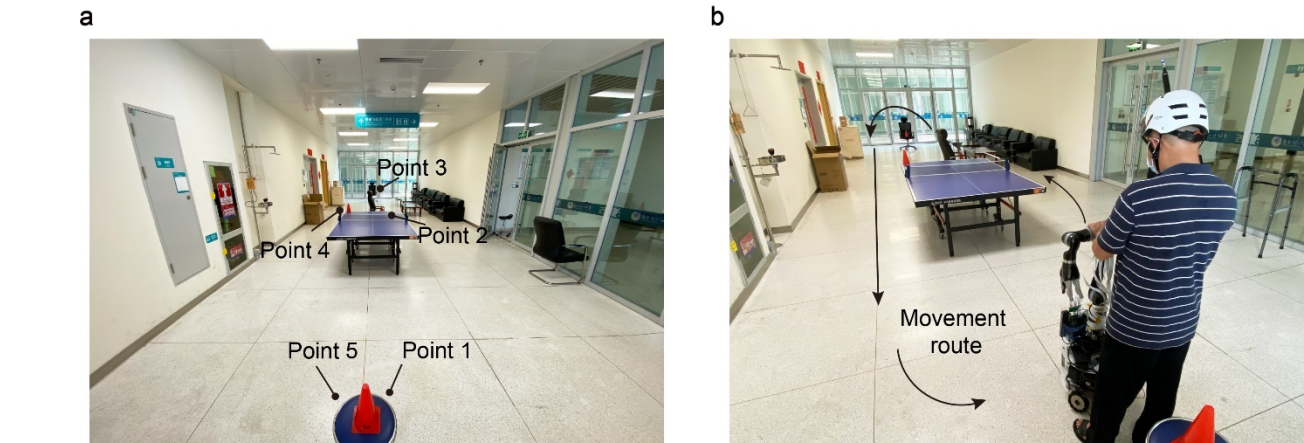
2 **Supplementary Figure 40. Temperature data distribution comparison between human touch**
3 **and non-human touch conditions for 12 subjects.** The lowest 5th percentile of the human body

4 temperature response is used as the threshold for triggering motion control.

5



2 **Supplementary Figure 41. Flowchart of the robot motion control system.** The system performs
3 admittance control by perceiving bimodal skin signals, ensuring appropriate human assistance and
4 the detection of emergency braking.
5



2 **Supplementary Figure 42. The schematic diagram of the experimental site for assisted**
3 **mobility of subject. (a)** Position markers for the target points in the mobile experiment. **(b)** Photos
4 of the actual movement path.

1 **Supplementary Tables**

2

| Mechanism | Iontronic | Resistive | Capacitive | Piezoelectric | Triboelectric |
|-----------------------|-------------|-------------------|------------|---------------|---------------|
| Sensitivity | <i>High</i> | <i>Low/medium</i> | <i>Low</i> | <i>High</i> | <i>High</i> |
| Noise | <i>Low</i> | <i>High</i> | <i>Low</i> | <i>Low</i> | <i>Low</i> |
| Anti-interference | <i>High</i> | <i>High</i> | <i>Low</i> | <i>High</i> | <i>High</i> |
| Static force response | <i>Yes</i> | <i>Yes</i> | <i>Yes</i> | <i>No</i> | <i>No</i> |

3 **Supplementary Table 1. Comparison of different sensing mechanisms for artificial flexible
4 skin¹⁵.** In contrast, the ion-electronic sensing mechanism offers significant advantages, including
5 high sensitivity, low noise, strong anti-interference capability, and static response.

| Method | Intrinsic force sensing | Pressure resolution | Readout rate | Sensing channels | Pressure range |
|--|---|----------------------|------------------------|------------------|-----------------------|
| Six-axis force/torque (SARA) ^{16, 17} | <i>Relies on complex deep learning models to infer intrinsic force information.</i> | $\sim 0.1 \text{ N}$ | 8 kFPS | 6 | $\sim 10 \text{ kPa}$ |
| Six-axis force/torque (UR10e) ¹⁸ | No | 5 N | $\sim 500 \text{ FPS}$ | 6 | $\sim 10 \text{ kPa}$ |
| Six-axis force/torque (RFT64-6A01) ¹⁹ | <i>Intrinsic force sensing modeling is required.</i> | 0.08 N | 1 kFPS | 6 | $\sim 10 \text{ kPa}$ |
| Six-axis force/torque ⁵ | No | -- | -- | 6 | -- |
| Our iontronic skins | Yes | 0.01 N | 93 FPS | 768 | 1000 kPa |

1 **Supplementary Table 2. A comparative analysis of the application performance of our**
 2 **flexible iontronic skins and traditional rigid six-axis force/torque sensors for robotic**
 3 **multisensory perception.** Compared to the latter, our sensor offers distinct advantages, including
 4 intrinsic force sensing, high-pressure resolution, multidimensional feature detection, and a wide
 5 pressure sensing range.

6

| Lightweight neural network | $R^2(F_x)$ | $R^2(F_z)$ | $R^2(T_z)$ | R^2 (Average) | Params | FLOPs |
|---------------------------------------|------------------------------|------------------------------|------------------------------|-----------------------------------|---------------|--------------|
| MI-Transformer | 87.8% | 87.7% | 91.3% | 88.9% | 3.32 M | 3.31 M |
| MobileNetV2 ²⁰ | 73.1% | 72.1% | 79.4% | 74.9% | 2.23 M | 5.62 M |
| ShuffleNet ²¹ | 83.1% | 83.2% | 52.8% | 73.0% | 1.26 M | 2.69 M |
| MobileViT ²² | 89.50% | 87.90% | 87.30% | 88.3% | 3.37 M | 3.37 M |
| ResNet18 ²³ | 85.9% | 86.4% | 91.1% | 87.8% | 11.17 M | 382.36 M |

1 **Supplementary Table 3. Comparison of performance results for lightweight intent**
2 **prediction neural networks.** In comparison, our MI-Transformer achieves higher prediction
3 accuracy with lightweight computational requirements.

4

- 1 **Supplementary Movie 1.**
- 2 Real-time response demonstration of bimodal iontronic skins
- 3 **Supplementary Movie 2.**
- 4 Real-time multisensory response demonstration of our robot.
- 5 **Supplementary Movie 3.**
- 6 Pressure response of the robot under different touch actions.
- 7 **Supplementary Movie 4.**
- 8 Real-time motion intention prediction using the hybrid motion intention model (HMIM) and the
- 9 virtual mass model (VMM)
- 10 **Supplementary Movie 5.**
- 11 Demonstration of a motion control game based on iontronic skins.
- 12 **Supplementary Movie 6.**
- 13 Demonstration of providing mobility assistance to individuals with movement impairments.
- 14 **Supplementary Movie 7.**
- 15 Comparison between the proposed robot and traditional assistive tool.

1 **References**

- 2 1. Shi, J. et al. Embedment of sensing elements for robust, highly sensitive, and cross-talk-free
3 iontronic skins for robotics applications. *Sci. Adv.* **9**, eadf8831 (2023).
- 4 2. Li, Z. et al. Ultrafast readout, crosstalk suppression iontronic array enabled by frequency-coding
5 architecture. *npj Flex. Electron.* **8**, 9 (2024).
- 6 3. Cirillo, A., Ficuciello, F., Natale, C., Pirozzi, S. & Villani, L. A conformable force/tactile skin
7 for physical human–robot interaction. *IEEE Rob. Autom. Lett.* **1**, 41-48 (2015).
- 8 4. Kalinowska, A., Pilarski, P.M. & Murphey, T.D. Embodied communication: How robots and
9 people communicate through physical interaction. *Annu. Rev. Control Rob. Auton. Syst.* **6**, 205-
10 232 (2023).
- 11 5. Chuy, O.Y., Hirata, Y., Wang, Z. & Kosuge, K. A control approach based on passive behavior
12 to enhance user interaction. *IEEE Trans. Rob.* **23**, 899-908 (2007).
- 13 6. Andreetto, M. et al. Simulating passivity for robotic walkers via authority-sharing. *IEEE Rob.*
14 *Auton. Lett.* **3**, 1306-1313 (2018).
- 15 7. Chuy, O., Hirata, Y. & Kosuge, K. in 2004 IEEE/RSJ International Conference on Intelligent
16 Robots and Systems (IROS)(IEEE Cat. No. 04CH37566), Vol. 3 2289-2294 (IEEE, 2004).
- 17 8. Fairbanks, B.D., Love, D.M. & Bowman, C.N. Efficient Polymer - Polymer Conjugation via
18 Thiol - ene Click Reaction. *Macromol. Chem. Phys.* **218**, 1700073 (2017).
- 19 9. Decker, C. & Decker, D. Photoinitiated radical polymerization of vinyl ether-maleate systems.
20 *Polymer* **38**, 2229-2237 (1997).
- 21 10. McHugh, P.J. et al. An Investigation of a (vinylbenzyl) trimethylammonium and N-
22 vinylimidazole-substituted poly (vinylidene fluoride-co-hexafluoropropylene) copolymer as an
23 anion-exchange membrane in a lignin-oxidising electrolyser. *Membranes* **11**, 425 (2021).
- 24 11. Mukhopadhyay, S. et al. Synthesis, characterization and properties of self-healable ionomeric
25 carboxylated styrene–butadiene polymer. *J. Mater. Sci.* **54**, 14986-14999 (2019).
- 26 12. Wong, D.H. et al. Nonflammable perfluoropolyether-based electrolytes for lithium batteries.
27 *Proceedings of the National Academy of Sciences* **111**, 3327-3331 (2014).
- 28 13. Tran, D., Bourdev, L., Fergus, R., Torresani, L. & Paluri, M. in Proceedings of the IEEE
29 international conference on computer vision 4489-4497 (2015).
- 30 14. Tran, D., Ray, J., Shou, Z., Chang, S.-F. & Paluri, M. Convnet architecture search for
31 spatiotemporal feature learning. *arXiv preprint arXiv:1708.05038* (2017).
- 32 15. Chang, Y. et al. First decade of interfacial iontronic sensing: from droplet sensors to artificial
33 skins. *Adv. Mater.* **33**, 2003464 (2021).

- 1 16. Iskandar, M., Albu-Schäffer, A. & Dietrich, A. Intrinsic sense of touch for intuitive physical
2 human-robot interaction. *Sci. Rob.* **9**, eadn4008 (2024).
- 3 17. Iskandar, M. et al. in 2020 IEEE/RSJ International Conference on Intelligent Robots and
4 Systems (IROS) 8903-8910 (IEEE, 2020).
- 5 18. Bolli, R., Bonato, P. & Asada, H.H. in 2023 IEEE/RSJ International Conference on Intelligent
6 Robots and Systems (IROS) 122-129 (IEEE, 2023).
- 7 19. Kim, U. et al. A novel intrinsic force sensing method for robot manipulators during human–
8 robot interaction. *IEEE Trans. Rob.* **37**, 2218-2225 (2021).
- 9 20. Sandler, M., Howard, A., Zhu, M., Zhmoginov, A. & Chen, L.-C. in Proceedings of the IEEE
10 conference on computer vision and pattern recognition 4510-4520 (2018).
- 11 21. Zhang, X., Zhou, X., Lin, M. & Sun, J. in Proceedings of the IEEE conference on computer
12 vision and pattern recognition 6848-6856 (2018).
- 13 22. Mehta, S. & Rastegari, M. Mobilevit: light-weight, general-purpose, and mobile-friendly
14 vision transformer. *arXiv preprint arXiv:2110.02178* (2021).
- 15 23. He, K., Zhang, X., Ren, S. & Sun, J. in Proceedings of the IEEE conference on computer vision
16 and pattern recognition 770-778 (2016).
- 17